ARTICLES

nature
structural &
molecular biology

Crystal structure of a chaperone complex that contributes to the assembly of yeast 20S proteasomes

Hideki Yashiroda[1,10], Tsunehiro Mizushima[2,10], Kenta Okamoto[3], Tomie Kameyama[1], Hidemi Hayashi[4,5], Toshihiko Kishimoto[5,6], Shin-ichiro Niwa[4], Masanori Kasahara[7], Eiji Kurimoto[3], Eri Sakata[1,3], Kenji Takagi[2], Atsuo Suzuki[2], Yuko Hirano[1], Shigeo Murata[1,8], Koichi Kato[3,9], Takashi Yamane[2] & Keiji Tanaka[1]

Eukaryotic 20S proteasomes are composed of two α-rings and two β-rings, which form an αββα stacked structure. Here we describe a proteasome-specific chaperone complex, designated Dmp1–Dmp2, in budding yeast. Dmp1–Dmp2 directly bound to the α5 subunit to facilitate α-ring formation. In Δ*dmp1* cells, α-rings lacking α4 and decreased formation of 20S proteasomes were observed. Dmp1–Dmp2 interacted with proteasome precursors early during proteasome assembly and dissociated from the precursors before the formation of half-proteasomes. Notably, the crystallographic structures of Dmp1 and Dmp2 closely resemble that of PAC3—a mammalian proteasome-assembling chaperone; nonetheless, neither Dmp1 nor Dmp2 showed obvious sequence similarity to PAC3. The structure of the Dmp1–Dmp2–α5 complex reveals how this chaperone functions in proteasome assembly and why it dissociates from proteasome precursors before the β-rings are assembled.

The 26S proteasome is a large protein complex consisting of a catalytic core particle (the 20S proteasome) and the 19S regulatory particle[1,2]. The 20S proteasome is a cylindrical particle formed by the axial stacking of four heteroheptameric rings: two outer α-rings and two inner β-rings, each of which is made up of seven structurally similar α and β subunits, respectively, interact to create a $\alpha_{1-7}\beta_{1-7}\beta_{1-7}\alpha_{1-7}$ structure.

The molecular mechanisms underlying the assembly of 20S proteasomes have attracted a great deal of interest in recent years. The proteasome from the archaebacterium *Thermoplasma acidophilum* has a quaternary structure that is essentially identical to that of eukaryotic proteasomes, although it is composed of only two different subunits, α and β. Coexpression of these subunits in *Escherichia coli* results in complete and proteolytically active proteasomes[3]. Although deletion of the propeptide of the β subunit has no effect on proteasome assembly in *T. acidophilum*, the assembly of the 20S proteasome in eukaryotes is more complicated; five of the seven β subunits (β1, β2, β5, β6 and β7) are synthesized as precursor forms with extended polypeptide sequences at their N termini, and the propeptides of the β subunits are required for eukaryotic 20S proteasomes to assemble normally[4].

Recent evidence indicates that proteasome assembly in eukaryotes requires additional chaperone molecules. In mammals, a heterodimer of proteasome-assembling chaperones 1 and 2 (PAC1-PAC2) binds to early assembly intermediates containing a restricted subset of α subunits and promotes α-ring formation[5]. PAC1-PAC2 remains attached to the α-ring after its formation and suppresses nonproductive α-ring dimerization, thereby promoting attachment of the β subunits to the α-rings. β subunits are thought to attach to the α-rings in an orderly manner in mammals as well as in yeast; in fact, incomplete precursor complexes consisting of all seven α subunits and three β subunits (β2, β3 and β4) have been identified[6,7]. Another chaperone molecule, known as the proteasome maturation factor Ump1, associates with 15S proteasome precursors[8]. In the yeast Δ*ump1* mutant, proteasome assembly and maturation are strongly impaired. In a similar way to PAC1-PAC2, a newly identified mammalian chaperone, PAC3, was also found to bind to the α-ring and to be required for proper α-ring formation[9]. Unlike PAC1-PAC2 and Ump1, however, PAC3 dissociates before the formation of half-proteasomes, a process that is coupled with the recruitment of the β subunits and Ump1.

Whether eukaryotic cells share a common mechanism for proteasome assembly is unknown. Yeast cells express Ump1 with about 30% amino acid sequence identity with the human counterpart (also called POMP and proteassemblin)[10–12], suggesting that Ump1 is probably conserved in eukaryotes. As for the PAC proteins, it was recently

[1]Laboratory of Frontier Science, Core Technology and Research Center, Tokyo Metropolitan Institute of Medical Science, Bunkyo-ku, Tokyo 113-8613, Japan. [2]Department of Biotechnology, Graduate School of Engineering, Nagoya University, Chikusa-ku, Nagoya 464-8603, Japan. [3]Department of Structural Biology and Biomolecular Engineering, Graduate School of Pharmaceutical Sciences, Nagoya City University, 3-1 Tanabe-dori, Mizuho-ku, Nagoya 467-8603, Japan. [4]Link Genomics, Inc., Chuo-ku, Tokyo 103-0024, Japan. [5]Proteome Analysis Center and [6]Department of Biomolecular Science, Faculty of Science, Toho University, Funabashi, Chiba 274-8510, Japan. [7]Department of Pathology, Hokkaido University Graduate School of Medicine, Sapporo, Hokkaido 060-8638, Japan. [8]Laboratory of Protein Metabolism, Graduate School of Pharmaceutical Sciences, the University of Tokyo, 7-3-1 Hongo, Bunkyo-ku, Tokyo 113-0033, Japan. [9]Institute for Molecular Science, National Institutes of Natural Sciences, 5-1 Higashi-yama, Myodaiji, Okazaki 444-8787, Japan. [10]These authors contributed equally to this work. Correspondence should be addressed to K. Tanaka (tanakak@rinshoken.or.jp).

Received 20 August 2007; accepted 9 January 2008; published online 17 February 2008; doi:10.1038/nsmb.1386

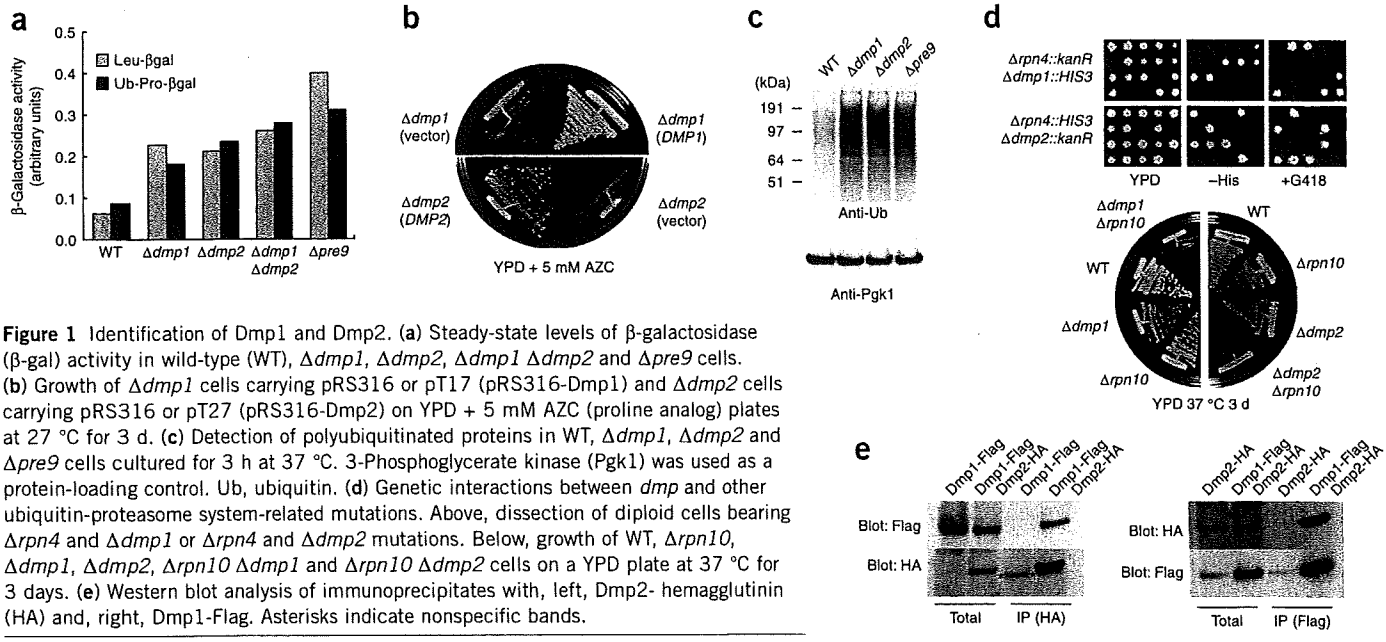

Figure 1 Identification of Dmp1 and Dmp2. (**a**) Steady-state levels of β-galactosidase (β-gal) activity in wild-type (WT), Δ*dmp1*, Δ*dmp2*, Δ*dmp1* Δ*dmp2* and Δ*pre9* cells. (**b**) Growth of Δ*dmp1* cells carrying pRS316 or pT17 (pRS316-Dmp1) and Δ*dmp2* cells carrying pRS316 or pT27 (pRS316-Dmp2) on YPD + 5 mM AZC (proline analog) plates at 27 °C for 3 d. (**c**) Detection of polyubiquitinated proteins in WT, Δ*dmp1*, Δ*dmp2* and Δ*pre9* cells cultured for 3 h at 37 °C. 3-Phosphoglycerate kinase (Pgk1) was used as a protein-loading control. Ub, ubiquitin. (**d**) Genetic interactions between *dmp* and other ubiquitin-proteasome system-related mutations. Above, dissection of diploid cells bearing Δ*rpn4* and Δ*dmp1* or Δ*rpn4* and Δ*dmp2* mutations. Below, growth of WT, Δ*rpn10*, Δ*dmp1*, Δ*dmp2*, Δ*rpn10* Δ*dmp1* and Δ*rpn10* Δ*dmp2* cells on a YPD plate at 37 °C for 3 days. (**e**) Western blot analysis of immunoprecipitates with, left, Dmp2- hemagglutinin (HA) and, right, Dmp1-Flag. Asterisks indicate nonspecific bands.

reported that in *Saccharomyces cerevisiae* Pba1 and Pba2, which show weak sequence similarity to PAC1 and PAC2, respectively, form a heterodimeric complex and bind to proteasome precursor complexes[7]. Unlike the phenotypes observed following PAC1 and PAC2 knockdowns, however, Δ*pba1* and Δ*pba2* cells show only mild defects in proteasome biogenesis.

In this paper, we describe a newly identified heterodimeric complex of Dmp1–Dmp2. Although Dmp1 and Dmp2 show no obvious sequence similarities to PAC3, the biological function and quaternary structure of this heterodimer are strikingly similar to those of PAC3. We show that Dmp1–Dmp2 is critically involved in 20S proteasome assembly, and we propose that the identified chaperone-dependent mechanisms that contribute to proteasome assembly are probably conserved among eukaryotes.

RESULTS

Isolation of *dmp* mutants

To search for genes involved in the ubiquitin-proteasome system, we streaked yeast knockout strains on YPD plates containing the proline analog L-azetidine-2-carboxylic acid (AZC; 5 mM) or SD plates containing the arginine analog canavanine (1 mg ml^{-1}) and incubated them at 26 °C for 3 d. Among the many mutants that were sensitive to the amino acid analogs, we selected 23 uncharacterized mutants on the basis of the criterion that the disrupted gene products or proteins that they interact with are conserved in higher eukaryotes. We then examined the ability of each mutant to degrade model substrates for the N-end rule pathway or the ubiquitin fusion degradation (UFD) pathway[13,14]. Because Δypl144w cells showed the most severe defect among the 23 selected mutants, we further examined the Δypl144w strain, which we named Δ*dmp1* (for degradation of misfolded proteins 1; **Fig. 1a**, **Supplementary Methods** and **Supplementary Fig. 1** online). We confirmed degradation defects in Δ*dmp1* cells by cycloheximide-chase experiments of Gcn4, a transcription activator that turns over rapidly in rich medium[15] (**Supplementary Fig. 1**). We cloned the YPL144W gene, including the 5′ and 3′ flanking regions, into the pRS316 single-copy vector. Because cloned YPL144W complemented the growth defect of the Δ*dmp1* cells on YPD + 5 mM AZC plates, we concluded that YPL144W was *DMP1* (**Fig. 1b**), which encodes a 148-residue (16.6 kDa) protein. We also confirmed that deletion of *DMP1* resulted in the stabilization of model substrates in another background strain, W303 (**Supplementary Fig. 1**).

Next we examined the accumulation of polyubiquitinated proteins in the Δ*dmp1* mutant. We used Δ*pre9* cells, which lacked the α3 subunit of the 20S proteasome, as a positive control. A larger amount of polyubiquitinated proteins accumulated in Δ*dmp1* cells than in wild-type cells, whereas the levels in Δ*dmp1* and Δ*pre9* cells were comparable (**Fig. 1c**). This result indicated that the ubiquitin-dependent degradation mediated by the 26S proteasome was impaired in Δ*dmp1* cells.

To further confirm that Dmp1 is involved in the ubiquitin-proteasome pathway, we crossed the Δ*dmp1* strain with strains carrying mutations affecting the ubiquitin-proteasome system. Rpn4 (also known as Son1 or Ufd5) is a transcriptional activator of genes encoding proteasome subunits[16,17], whereas Rpn10 (the mammalian S5a homolog) acts as a receptor capable of trapping polyubiquitinated proteins[18]. When we crossed Δ*dmp1* with Δ*rpn4*, no double mutants were obtained from 6 predicted tetratypes and 2 nonparental ditypes in tetrad analysis of 11 asci (**Fig. 1d** and data not shown). In contrast, Δ*dmp1* Δ*rpn10* double mutants were viable, but showed synthetic growth defects at high temperatures (**Fig. 1d**). These genetic interactions suggested that the ubiquitin-proteasome pathway was impaired in Δ*dmp1* cells.

Identification of Dmp1-interacting proteins

To identify proteins that interact with Dmp1, we generated a strain expressing C-terminally Flag-tagged Dmp1 from its native promoter and analyzed anti-Flag immunoprecipitates using MS. We identified three interacting proteins: one previously unknown protein encoded by YLR021W as well as the α5 (Pup2) and α6 (Pre5) subunits of the 20S proteasome (**Supplementary Fig. 2** online). Because the disruptant of the previously unknown protein displayed AZC sensitivity similar to the Δ*dmp1* strain, we named the YLR021W gene product Dmp2 (**Fig. 1b**). Dmp2 consists of 179 amino acid residues and has a molecular mass of 20.1 kDa. In addition to AZC sensitivity,

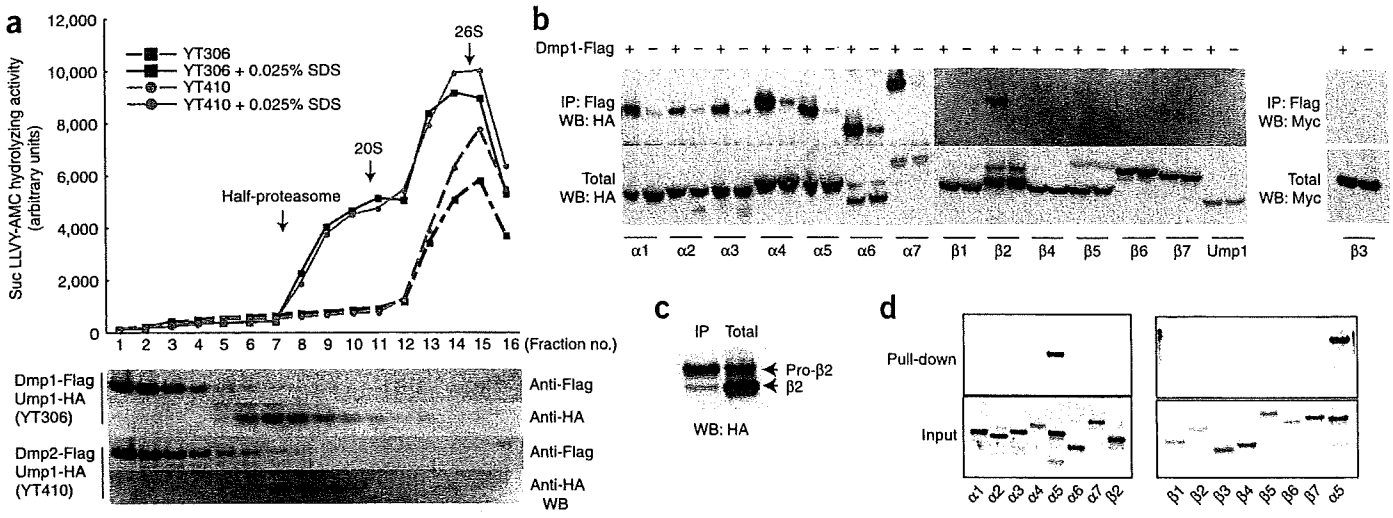

Figure 2 Characterization of the Dmp1–Dmp2 complex. (**a**) Suc-LLVY-AMC hydrolyzing activity of cell lysates fractionated by glycerol gradient centrifugation (above) and immunoblotted (WB) with anti-Flag or anti-hemagglutinin (HA) antibodies (below). The three arrows depict the locations of half-proteasomes, 20S proteasomes and 26S proteasomes. (**b**) Detection of coimmunoprecipitated (IP) proteasome subunits with Dmp1-Flag. (**c**) Comparison of the β2 subunit in the total lysate or immunoprecipitate with Dmp1-Flag. (**d**) Binding assay of recombinant GST-Dmp1–Dmp2 and the 20S proteasome subunits translated and ^{35}S-radiolabeled in reticulocyte lysates.

Δ*dmp2* cells showed the same phenotypes as Δ*dmp1* cells, including the stabilization of model substrates and accumulation of polyubiquitinated proteins (**Fig. 1a,c**). Furthermore, we observed synthetic lethality and high temperature sensitivity when Δ*dmp2* cells were crossed with Δ*rpn4* and Δ*rpn10* cells, respectively (**Fig. 1d**).

Next, to examine the interaction between Dmp1 and Dmp2 *in vivo*, Dmp2 was C-terminally tagged with hemagglutinin (HA). Dmp2-3×HA was immunoprecipitated from cell extracts using anti-HA antibodies. Western blots of the immunoprecipitated material using anti-Flag antibodies revealed that Dmp1-3×Flag was also present (**Fig. 1e**). Conversely, when Dmp1-3×Flag was immunoprecipitated using anti-Flag antibodies, Dmp2-3×HA was coimmunoprecipitated (**Fig. 1e**). To further confirm that Dmp1 and Dmp2 form a complex, 6×His-Dmp1 and Dmp2 were coexpressed in *E. coli* and purified using nickel-agarose beads. Dmp1 and Dmp2 formed a complex with an apparent 1:1 stoichiometry and a relative molecular mass of 43 kDa, indicating that the complex was a heterodimer (**Supplementary Fig. 3** online).

We then examined whether the Δ*dmp1* phenotype was enhanced by the deletion of *DMP2*. The Δ*dmp1* Δ*dmp2* double mutant was viable, and, compared to the single mutants, the double deletion did not enhance the stabilization of model substrates (**Fig. 1a**). This result implies that Dmp1 and Dmp2 function as a complex, and that the deletion of either protein was sufficient to eliminate the function of the heterodimeric complex.

Dmp1–Dmp2 binds to 20S proteasome precursors

To further characterize the interaction between Dmp1–Dmp2 and the proteasome subunits, cell extracts of strains expressing Ump1-HA and Dmp1-3×Flag or Dmp2-3×Flag were fractionated using 8–32% (v/v) glycerol density-gradient centrifugation. The Dmp1–Dmp2 complex and half-proteasomes containing Ump1 were detected on western blots using anti-Flag and anti-HA antibodies (**Fig. 2a**, below). Peptidase activity in each fraction was also measured to determine the distributions of the 20S and 26S proteasomes (**Fig. 2a**, above). A low concentration of SDS (0.025% (w/v)) is known to act as an artificial activator of 20S proteasomes that are usually latent in cells. This allowed us to discriminate the activity of 20S proteasomes from that of 26S proteasomes. Both Dmp1-3×Flag and Dmp2-3×Flag were primarily observed in fractions 1–4, whereas Ump1-HA was found in fractions 7–10, and 20S and 26S proteasomes were identified in fractions 10–12 and 14–15, respectively. This result indicates that the Dmp1–Dmp2 complex does not bind to the α subunits either in the half-proteasomes or in mature proteasomes.

To examine whether the Dmp1–Dmp2 complex bound specifically to α5 and α6 *in vivo*, all of the α and β subunits except β3 and Ump1 were C-terminally tagged with HA. Adding a 3×HA tag onto the C terminus of β3 caused lethality, so we constructed a strain expressing N-terminally Myc-tagged β3 under the control of the *GAL1* promoter. As shown in **Figure 2b**, when Dmp1-3×Flag was immunoprecipitated using anti-Flag M2 agarose beads, all of the α subunits were pulled down with Dmp1-3×Flag. In contrast, of the β subunits, only β2 was pulled down. Intriguingly, β2 coimmunoprecipitated as its precursor form, which was verified by comparing the coimmunoprecipitated form with β2 in the total cell lysate (**Fig. 2c**). No interaction between Ump1 and Dmp1 was detected (**Fig. 2b**). These results indicate that assembly of the 20S proteasome proceeds via a precursor complex composed of the α-ring, β2 and Dmp1–Dmp2, and that the Dmp1–Dmp2 complex dissociates from precursors before the formation of half-proteasomes containing Ump1.

We then investigated which of the proteasome subunits bind directly to Dmp1–Dmp2. Glutathione S-transferase (GST)–tagged Dmp1–Dmp2 (GST–Dmp1–Dmp2) bound to only the α5 subunit among the α and β subunits, and Ump1 translated *in vitro* (**Fig. 2d**). This result indicated that the Dmp1–Dmp2 complex bound to the proteasome precursors via direct interactions with the α5 subunit.

Impairment of 20S proteasome assembly in Δ*dmp1* cells

We then examined the Δ*dmp1* phenotype in more detail, focusing on proteasome biogenesis. Extracts from wild-type or Δ*dmp1* cells were fractionated using 8–32% (v/v) glycerol gradient centrifugation, and the peptidase activity of each fraction was measured with or without 0.025% (w/v) SDS (**Fig. 3a**). This experiment revealed that the 20S proteasome activity was reduced by approximately 60% in Δ*dmp1*

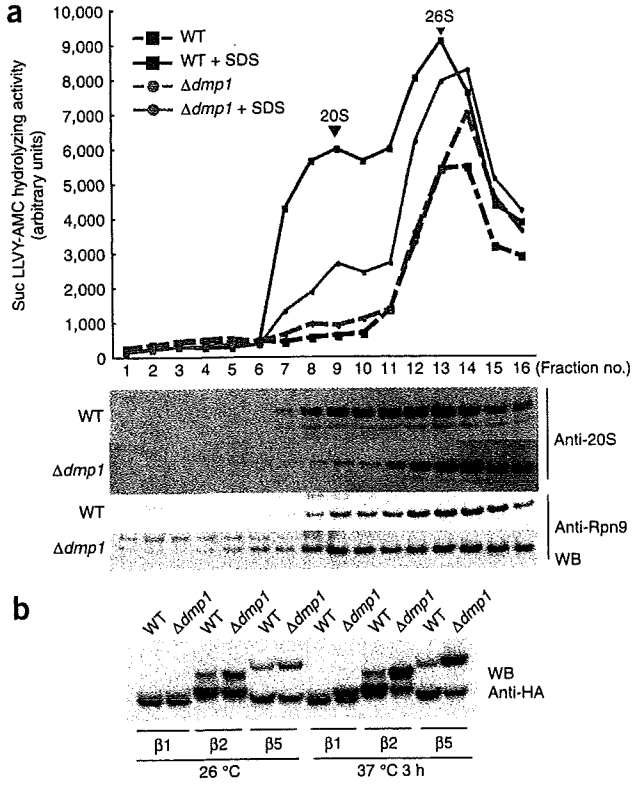

Figure 3 Impaired 20S proteasome assembly in Δ*dmp1* cells. (**a**) Suc-LLVY-AMC hydrolyzing activity of proteasomes in wild-type (WT) and Δ*dmp1* cells and immunoblotted (WB) with anti-20S (above) or anti-Rpn9 (below) antibodies. Arrowheads indicate the positions of 20S or 26S proteasomes. (**b**) WB analysis of HA-tagged β subunits in WT and Δ*dmp1* cells.

cells compared to wild-type cells. Immunoblot analysis using an antibody to yeast 20S confirmed that the level of 20S proteasome was lower in Δ*dmp1* cells (**Fig. 3a**, below). For Δ*dmp1* cells, the bands representing the 20S proteasome were faint in fractions 7–10. Conversely, the bands representing the lid component Rpn9 were slightly stronger in the fractions from Δ*dmp1* cells than in those from wild-type cells (**Fig. 3a**, below). The level of free 19S regulatory particle complexes may have increased in Δ*dmp1* cells as a result of the shortage of 20S proteasomes.

The impairment of 20S proteasome assembly in Δ*dmp1* cells was supported by the observation that the propeptides of the β subunits were not efficiently cleaved in these cells. This phenotype was more apparent at elevated temperatures (**Fig. 3b**).

Dmp1–Dmp2 is involved in α-ring formation

We further examined the involvement of the Dmp1–Dmp2 complex in proteasome biogenesis. Total cell lysates from wild-type, Δ*dmp1*, Δ*dmp2*, Δ*blm10* and Δ*pba2* cells were subjected to blue native PAGE (BN-PAGE) (**Fig. 4a**). Blm10 has been reported to be involved in a late stage of nuclear proteasome assembly and to function as a proteasome activator, although these findings remain controversial[19,20]. Pba2 has weak amino acid–sequence similarity to mammalian PAC2 (refs. 5,7). In agreement with the decreased 20S proteasome activity (**Fig. 3a**), the level of 20S proteasomes was lower in Δ*dmp1* and Δ*dmp2* cells, whereas no appreciable decrease was observed for Δ*pba2* or Δ*blm10* cells. Notably, in addition to the decrease in the level of 20S proteasomes, we observed other quickly migrating bands in the samples from Δ*dmp1* and Δ*dmp2* cells. To identify these bands, we carried out BN-PAGE and western blot analysis using strains expressing HA-tagged proteasome subunits. The results revealed that the quickly migrating bands contained all of the α subunits except α4, together with β2 (**Fig. 4b**). Tagging β6 with HA seemed to affect the assembly of the 20S proteasome, because the resulting band pattern was different from those observed from the strains expressing other tagged subunits (data not shown). Furthermore, it is noteworthy that anti-HA antibodies did not recognize the α7 subunit in mature proteasomes, whereas it clearly stained the subunit in the intermediate band, suggesting that the C-terminal portion of the α7 subunit is cleaved during maturation of the β-ring. To confirm that α4 was not part of the quickly migrating band observed in samples from Δ*dmp1* cells and to eliminate the possibility

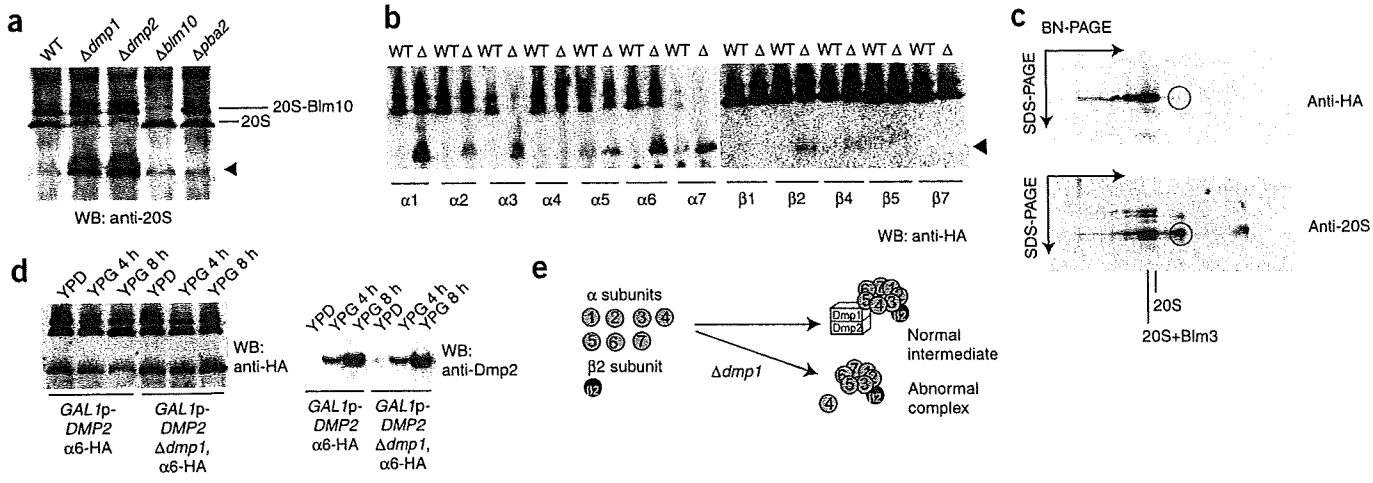

Figure 4 Detection of abnormal α-rings lacking α4 in Δ*dmp1* and Δ*dmp2* cells. Blue native (BN)-PAGE and immunoblotting (WB) with anti-20S proteasome (**a**) or anti- hemagglutinin (HA) antibodies (**b**). The filled arrowhead denotes intermediates composed of α-rings observed in Δ*dmp1* and Δ*dmp2* cells. Δ in **b** denotes Δ*dmp1*. Note in **b** that the C-terminally attached HA tag of α7 may not be present in mature proteasomes in both wild-type (WT) and Δ*dmp1* cells. (**c**) Two-dimensional BN–SDS-PAGE analysis of the proteasome in YT334 (Δ*dmp1*, α4-HA) cells. Circles denote the position of a quickly migrating band observed only in Δ*dmp1* and Δ*dmp2* cells. (**d**) Detection of abnormal complex by BN-PAGE and immunoblotting (left). Detection of Dmp2 by SDS-PAGE and immunoblotting (right). (**e**) Schematic model for Dmp1–Dmp2 function. Dmp1–Dmp2 is required for the efficient construction of the α-ring. The details of the model are provided in the text.

that the HA epitope of α4-HA was buried and inaccessible to the anti-HA antibodies, we conducted two-dimensional BN-PAGE–SDS-PAGE; the results confirmed that α4 was indeed absent from this complex (**Fig. 4c**). We then examined whether this complex was a normal intermediate or an abnormal complex using the strains in which *DMP2* is under the control of the galactose-inducible promoter. When the expression of *DMP2* was repressed in YPD medium, quickly migrating bands were observed as expected (**Fig. 4d**). If this complex is a normal intermediate, which can be detected only when the assembly step is slowed by the lack of Dmp2, it is expected to be diminished promptly when the Dmp2 proteins are supplied again. However, this complex remained even 4 h after the expression of *DMP2* was induced (**Fig. 4d**). This result suggests that the lack of Dmp1–Dmp2 results in nonproductive complexes and that the Dmp1–Dmp2 complex ensures that the steps underlying proteasome assembly occur in the proper order (**Fig. 4e**). Dmp1–Dmp2 is required for the efficient construction of α-rings and in particular for the incorporation of α4 into the α-rings.

Overall structure of the Dmp1–Dmp2 complex

To examine the structural basis of the function of this chaperone, the crystal structure of the Dmp1–Dmp2 complex was determined using multiwavelength anomalous dispersion and refined to 1.96-Å resolution (**Fig. 5a**). Dmp1 has a globular structure consisting of a six-stranded β-sheet and three α-helices. Two antiparallel sheets ($S_1$1, $S_1$2, $S_1$3 and $S_1$4, $S_1$5, $S_1$6) are composed of three β-strands joined by a parallel interaction between one strand from each sheet ($S_1$3 and $S_1$6). $H_1$1 and $H_1$3 are bound on one side of the β-sheet, and one short helix ($H_1$2) is located between $S_1$6 and $H_1$3. Dmp2, which has a globular structure similar to that of Dmp1, consists of a six-stranded β-sheet and four α-helices. Although no obvious amino acid–sequence similarity between Dmp1 and Dmp2 was observed, the tertiary structure of Dmp2 closely resembles that of Dmp1, with an average r.m.s. deviation of 3.0 Å for 103 Cα atoms (**Fig. 5a**). The loop between $S_1$4 and $S_1$5 of Dmp1 (residues 68–77), however, is distinct from the same loop in Dmp2 (residues 60–90 between $S_2$4 and $S_2$5 of Dmp2). The loop in Dmp2 is larger than that in Dmp1 and is part of a protruding structure that also contains $H_2$1 and a flexible region. The $H_2$1 helix is stabilized by a crystal contact.

The Dmp1–Dmp2 heterodimer has a β-sandwich structure formed by two six-stranded β-sheets consisting of strands $S_1$1–$S_1$6 of Dmp1 and $S_2$1–$S_2$6 of Dmp2 (**Fig. 5a,b**). This sandwich structure is surrounded by helices $H_1$1 and $H_1$3 of Dmp1 on one side and $H_2$2 and $H_2$4 of Dmp2 on the other side. Dmp1 and Dmp2 interact through an extensive interface that is approximately 25 Å long and 22 Å wide, burying a total of 2,318 Å^2 of surface area (1,159 Å^2 each for Dmp1 and Dmp2). The interface involves β-strands $S_1$1-$S_1$6, loop $S_1$2-$S_1$3 and loop $S_1$3-$S_1$4 of Dmp1, which interact against β-strands $S_2$1-$S_2$6, loop $S_2$2-$S_2$3 and loop $S_2$3-$S_2$4 of Dmp2. Dmp1–Dmp2 binding is mediated by both hydrogen bonds and van der Waals contacts (**Fig. 5c**). Residues involved in intermolecular formation of hydrogen bonds are Leu2, Pro37, Ser39, Ser53, Ser54, Leu56, Tyr59 and Leu85 of Dmp1 (located in strands $S_1$1, $S_1$3, $S_1$4 and $S_1$5, and loop $S_1$3-$S_1$4) and Glu26, Asn35, Asn36, Gln41, Arg43, Lys100 and Ser144 of Dmp2 (located in strands $S_2$2, $S_2$3, $S_2$5 and $S_2$6, and loop $S_2$2 -$S_2$3). Although the interface residues are not well conserved between Dmp1 and Dmp2, they occupy similar positions in the three-dimensional structure of each Dmp molecule (**Fig. 5d**).

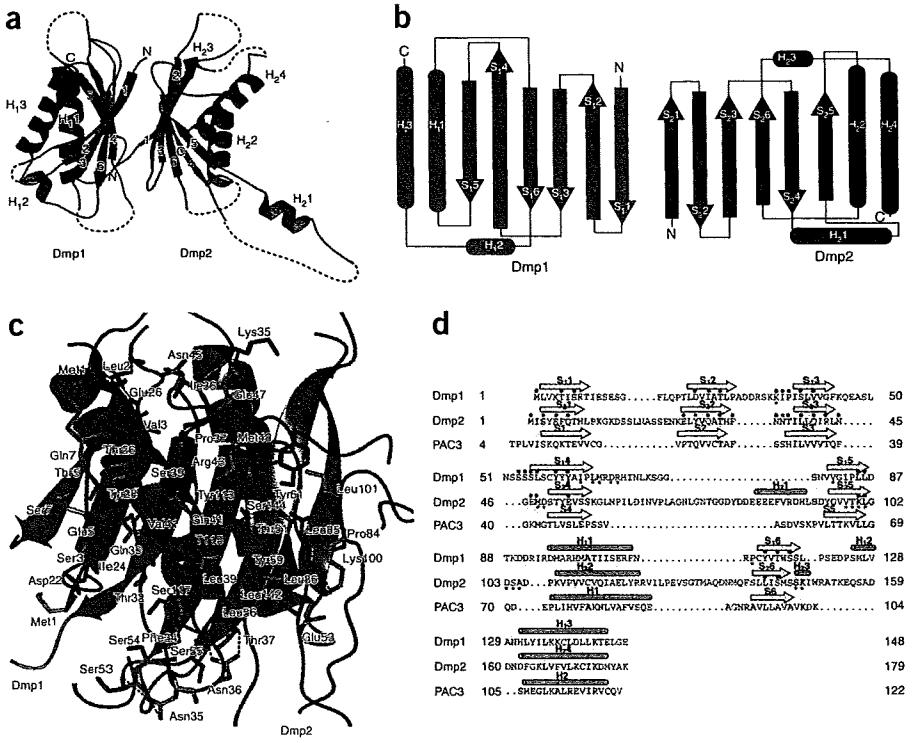

Figure 5 Structure of the Dmp1–Dmp2 complex. (**a**) A ribbon diagram of the Dmp1–Dmp2 complex. Dmp1 and Dmp2 are colored blue and red, respectively. The secondary structural elements are labeled. Dotted lines represent disordered regions. (**b**) Topology diagram of the Dmp1–Dmp2 complex. The α helices and β strands are represented by cylinders and arrows, respectively. (**c**) Close-up view of the Dmp1–Dmp2 interface showing amino acids of Dmp1 (blue) and Dmp2 (red). Hydrogen bonds are indicated by dotted lines. (**d**) Structure-based sequence alignments of Dmp1, Dmp2 and PAC3. The secondary structural elements of Dmp1, Dmp2 and PAC3 are indicated above the alignments. Identical or highly conserved residues are highlighted with a blue background. Residues that interact with Dmp2, Dmp1 and α5 are indicated by red dots, purple dots and green stars, respectively.

Structure of the Dmp1–Dmp2–α5 complex

The Dmp1–Dmp2 complex directly interacted with the α5 subunit (**Fig. 2d**). To understand the binding of Dmp1–Dmp2 to α5, we first constructed a mutant version of Dmp2 (Dmp2 Δloop), in which the protruding region (residues 61–90) was deleted to facilitate crystallization. The crystal structure of the Dmp1–Dmp2 Δloop–α5 complex was determined at 2.9-Å resolution (**Fig. 6a**, above). The structure of α5, which consists of five α-helices and ten β-strands, is essentially identical to the previously reported structure of the α5 subunit in the 20S proteasome complex; these structures have an average r.m.s. deviation of 0.79 Å for the Cα positions. The H0 helix of α5, however, is disordered in the Dmp1–Dmp2 Δloop-α5 complex (**Fig. 6a**, above). The Dmp1–Dmp2 Δloop structure in the Dmp1–Dmp2 Δloop–α5 complex can be superposed on the Dmp1–Dmp2 structure with an average r.m.s. deviation of 0.93 Å for the Cα positions, indicating that α5 binding does not cause substantial structural changes in the Dmp1–Dmp2 complex. The Dmp1–Dmp2 Δloop complex and

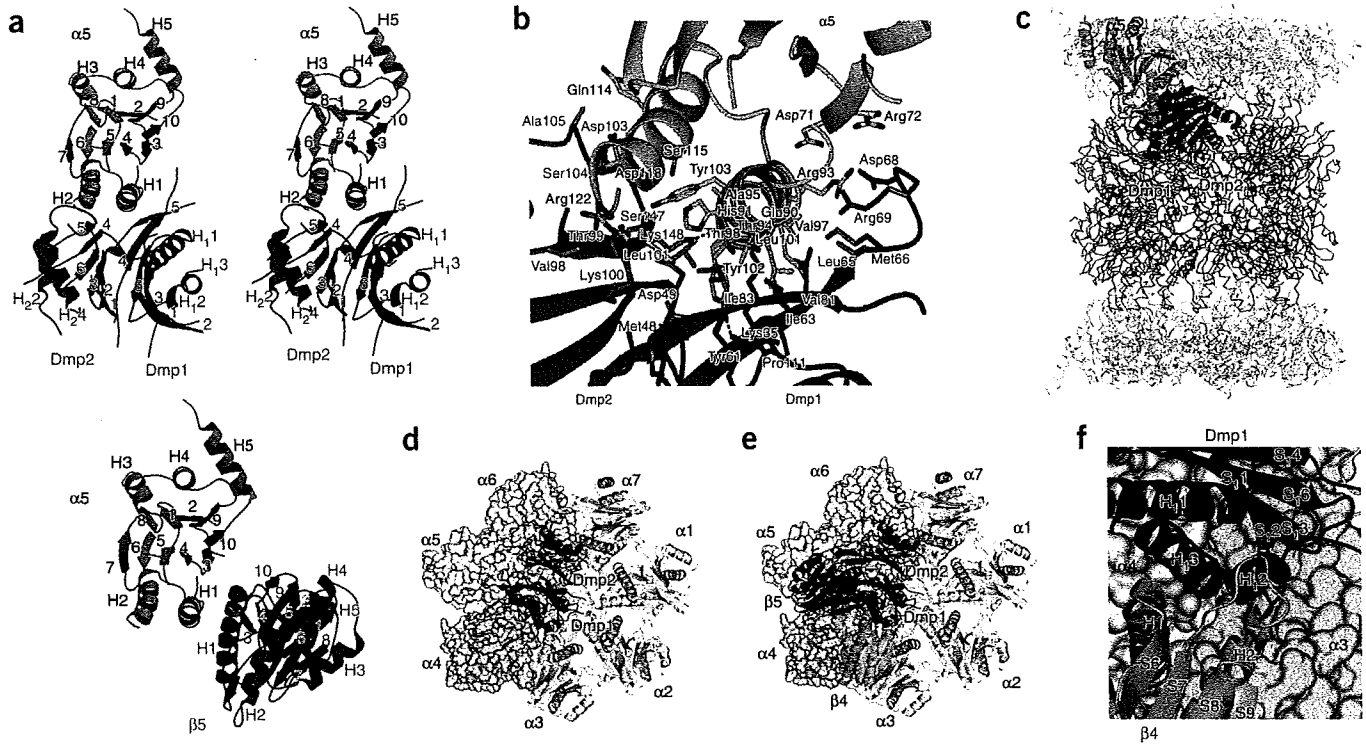

Figure 6 Structure of the Dmp1–Dmp2–α5 complex. (**a**) Above, a stereo ribbon diagram of the Dmp1–Dmp2 Δloop-α5 complex. Dmp1, Dmp2 Δloop and α5 are colored blue, red and cyan, respectively. Below, a ribbon diagram of the α5 (PDB ID code: 1RYP; chain E, cyan) and β5 (PDB ID code: 1RYP; chain L, green) complex. The secondary structural elements are labeled. (**b**) Close-up view of the Dmp1–Dmp2 Δloop–α5 interface showing amino acids of Dmp1 (blue), Dmp2 (red) and α5 (cyan). Hydrogen bonds are indicated by dotted lines. (**c**) Binding positions of the Dmp1–Dmp2 complex in the 20S proteasome. Dmp1, Dmp2 and α5 are shown as ribbon representations and are colored blue, red and cyan, respectively. Cα traces are colored yellow in the α-ring and green in the β-ring. (**d**) Model of the Dmp1–Dmp2–α-ring complex derived from the published structure of the yeast proteasome (PDB ID code: 1RYP). Dmp1, Dmp2 and the α-ring (α1, α2, α3 and α7) are shown as ribbon representations and are colored blue, red and yellow, respectively. α4 (violet), α5 (light yellow) and α6 (light blue) are shown as surface plots. (**e**) Model of the Dmp1–Dmp2–α-ring–β4–β5 complex. β4 and β5 are shown as ribbon representations and are colored light green and green, respectively. (**f**) Close-up view of the interface between Dmp1 and β4 in the model of the complex.

α5 are bound by interactions of $S_1$4, $S_1$5 and loops $S_1$2-$S_1$3, $S_1$4-$S_1$5, and $H_1$1-$S_1$6 of Dmp1; $H_2$3, $S_2$5 and loops $S_2$3-$S_2$4 and $S_2$5-$H_2$2 of Dmp2; and helices H1 and H2 of α5. The truncated loop of Dmp2 is located on the opposite side of α5. A total of 984 Å^2 of accessible surface area (557 Å^2 for Dmp1 and 427 Å^2 for Dmp2) is buried at the interface between the Dmp1–Dmp2 Δloop complex and α5. The α5 subunit binds to Dmp1–Dmp2 by packing its H1 helix against the concave surface of the Dmp1–Dmp2 complex (**Fig. 6a**, above, and **Fig. 6b**). The surface area occupied by the H1 helix of the Dmp1–Dmp2 complex is 692 Å^2. Glu90, Thr94, Val97, Leu101, Tyr102, Tyr103 and Arg122 of α5 have a central role, making multiple van der Waals contacts to Dmp1 and Dmp2. Thr94, Val97 and Tyr102 are not conserved among the α subunits of yeast proteasomes; these residues might be important for specific interactions between α5 and the Dmp1–Dmp2 complex. The intermolecular hydrogen bonds are formed by residues Tyr102, Tyr103, Asp118 and Arg122 of α5, Lys35 of Dmp1 and Met48, Thr99, Ser104, Ser147 and Lys148 of Dmp2.

The structure of the Dmp1–Dmp2 Δloop–α5 complex illustrates an intermediate state of proteasome assembly. A model of Dmp1–Dmp2 interacting with the α-ring was generated by superimposing the α5 subunit from Dmp1–Dmp2 Δloop–α5 on the structure of the 20S proteasome (PDB ID code 1RYP). In this model, Dmp1–Dmp2 bound to the inner surface of the α-ring (**Fig. 6c,d**). The Dmp1–Dmp2 binding sites in the α-ring are located more internally than those that interact with the β subunits (**Fig. 6e**). The β2, β3 and β4 subunits of the proteasomes are thought to attach to the α-rings during the primary stage of β-ring assembly. In the Dmp1–Dmp2–α-ring model, attachment of the β4 subunit to the α-ring causes steric hindrance between β4 and Dmp1 (**Fig. 6e,f**). This steric hindrance probably triggers the release of Dmp1–Dmp2 from the α-ring during the attachment of the β subunits onto the α-ring.

Structural similarity between Dmp1, Dmp2 and PAC3

The functional features of the Dmp1–Dmp2 complex discussed above are reminiscent of mammalian PAC3. PAC3 is involved in α-ring formation and is released from precursor complexes before the formation of half-proteasomes. To examine whether Dmp1–Dmp2 and PAC3 are structurally similar, we determined the crystal structure of PAC3 at 2.0-Å resolution. In the crystal, PAC3 forms a homodimer related by pseudo two-fold symmetry (**Fig. 7a**). Notably, the tertiary structure of PAC3 is strikingly similar to those of Dmp1 and Dmp2 (**Fig. 7b**). PAC3 assumes a fold composed of one six-stranded β-sheet and two α-helices: H1 and H2 (**Fig. 7c**). Superposition of PAC3 on Dmp1 and Dmp2 resulted in an average r.m.s. deviation of 3.2 Å for 107 Cα atoms and 2.0 Å for 111 Cα atoms, although no obvious sequence similarity was found even when the alignment was made on the basis of experimentally verified secondary structures (**Fig. 5d**). Comparison of the structures of Dmp1, Dmp2 and PAC3 with other known protein structures using the DALI server yielded no proteins with marked structural similarities.

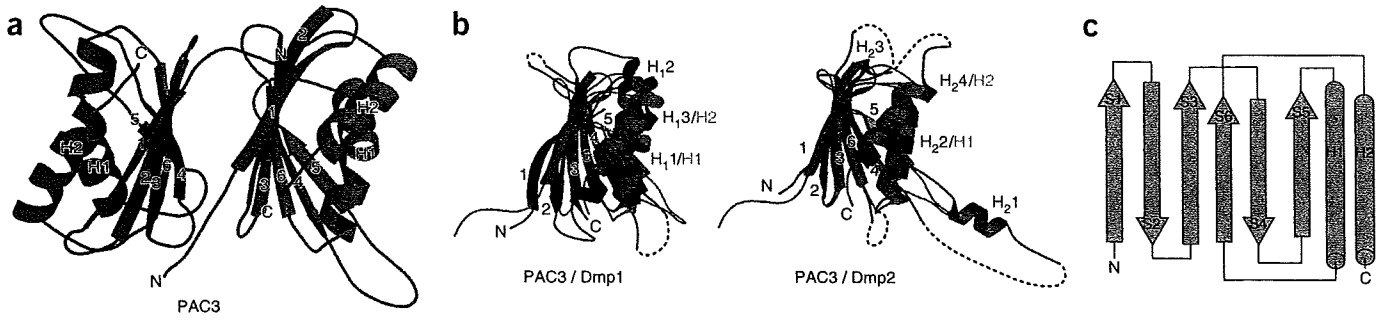

Figure 7 Structural similarity between Dmp1–Dmp2 and the human PAC3. (**a**) Structure of PAC3. A ribbon diagram of the PAC3 homodimer. Molecule A and molecule B are colored dark cyan and olive, respectively. The secondary structural elements of PAC3 are labeled. (**b**) The structure of PAC3 (olive) is compared with the structures of Dmp1 (blue) and Dmp2 (red). The secondary structural elements are labeled. (**c**) Topology diagram of PAC3. α-Helices and β-strands are represented by cylinders and arrows, respectively.

DISCUSSION

We have identified the Dmp1–Dmp2 complex as a proteasome-assembling chaperone in budding yeast. Dmp1–Dmp2 binds to proteasome subunits until they are organized into precursor complexes consisting of an α-ring and a β2 subunit and dissociates by the time the precursors become half-proteasomes, which consist of one copy of each α- and β-ring.

Whereas α-ring formation in mammals is driven by a concerted action of several chaperones (that is, the PAC1-PAC2 heterodimer and PAC3)[5,9], Dmp1 and Dmp2 are the first chaperone molecules shown to be involved in α-ring formation in yeast. Although neither Dmp1 nor Dmp2 is essential for normal growth, self-assembly of 20S proteasomes may be less efficient in the absence of Dmp1–Dmp2, particularly under stressful conditions. Supporting this idea, we detected α-rings lacking α4 in Δ*dmp1* cells but not in wild-type cells. Thus, we propose that the Dmp1–Dmp2 complex acts as a chaperone for α-ring formation (**Fig. 4e**). This complex may inhibit inappropriate binding between α3 and α5. It may also accelerate the incorporation of α4 into the α-ring. Lastly, Dmp1–Dmp2 may ensure proper β-ring assembly by masking specific docking sites on the β subunits (**Fig. 6d**) to help locate the β2 subunit at its proper position on the α-ring.

Is the function mediated by Dmp1–Dmp2 conserved in eukaryotes other than budding yeast? PAC3 shares many characteristics with Dmp1–Dmp2. In PAC3-knockdown cells, α-ring formation is impaired, leading to decreased synthesis of 20S proteasomes[9]. Disruption of Dmp1 or Dmp2 also results in decreased formation of 20S proteasomes. Unfortunately, we did not detect α-rings using glycerol gradient fractionation even in wild-type yeast cells, possibly because the assembly of the 20S proteasome occurs more rapidly in yeast than in mammals. We did, however, identify α-rings lacking α4 in Δ*dmp1* cells by BN-PAGE and western blot analysis (**Fig. 4**), indicating that, as does PAC3, Dmp1–Dmp2 has a crucial role in α-ring formation. Another feature shared by Dmp1–Dmp2 and PAC3 is that they dissociate before the formation of half-proteasomes, as is often the case with chaperone molecules.

Consistent with the functional similarities described above, X-ray structural analysis revealed that Dmp1, Dmp2 and PAC3 share extensive structural similarities. Interestingly, the overall structure of Dmp1–Dmp2 resembles those of 20S proteasome α and β subunits, although the two β-sheets in the α and β subunits are made up of five β-strands[21,22] (**Supplementary Fig. 4** online). Attachment of β5 to α5 is achieved via interactions between H1 of β5 and H1, S3 and a loop between S2 and S3 of α5 (**Fig. 6a**, below). We initially predicted that the Dmp1–Dmp2 complex would interact with α5 in a similar manner. Structural analysis, however, revealed that the binding mode of Dmp1–Dmp2 to α5 is different from that of β5 to α5 (**Fig. 6a**). In the Dmp1–Dmp2–α-ring model, Dmp1–Dmp2 is located more deeply within the α-ring, which allows Dmp1–Dmp2 to interact with α4, α5 and α6, whereas β5 interacts with only α4 and α5 (**Fig. 6e**). The unique binding mode of Dmp1–Dmp2 may be essential for its role as a proteasome-assembling chaperone.

The crystal structure of Dmp1–Dmp2–α5 also provided important insights into the molecular mechanism underlying the release of Dmp1–Dmp2 from the precursor complex. Dmp1–Dmp2 does not attach to the α-ring in the presence of β4 because of steric hindrance between β4 and Dmp1 (**Fig. 6e,f**). This model is consistent with our *in vivo* immunoprecipitation data showing that, among the β subunits, only β2 was coimmunoprecipitated with Dmp1–Dmp2 (**Fig. 2b**). Although no interaction was observed between Dmp1–Dmp2 and the β subunits *in vitro*, PAC3 directly binds to several β subunits *in vitro*. It is possible that transient and/or weak interactions with these β subunits trigger the release of PAC3 from the proteasome precursors.

In conclusion, we have demonstrated that, regardless of whether Dmp1–Dmp2 and PAC3 are evolutionarily related (**Supplementary Discussion** and **Supplementary Figs. 5** and **6** online), chaperones are likely to contribute to 20S proteasome assembly in all eukaryotes. Such mechanisms presumably became important as the 20S proteasome increased its structural complexity by acquiring seven distinct subunits for each ring.

During the preparation of this manuscript, Poc3 and Poc4 were reported to be yeast 20S proteasome assembling chaperones, which are identical to Dmp2 and Dmp1, respectively[23].

METHODS

Strains and plasmids. The *E. coli* strain DH5α was used for propagating plasmids. BL21 (DE3) cells were used for expression and purification of recombinant proteins. Strain genotypes are given in **Supplementary Table 1** online. Yeast knockout strains (catalogue number YSC1053) were purchased from Open Biosystems. The plasmids used in this study are listed in **Supplementary Table 2** online.

Immunological analysis. SDS-PAGE, BN-PAGE and western blotting were carried out with the NuPAGE system (Invitrogen) as per instructions provided by the manufacturer. Anti-Dmp2, anti-HA (Babco), anti-Flag (Sigma), anti-ubiquitin (Chemicon), anti-Pgk1 (Molecular Probe), anti-20S[24] and anti-Rpn9 (ref. 25) antibodies were used at various points during the course of this study. Anti-Dmp2 was raised in rabbits using recombinant Dmp1–Dmp2 complex. 6×His-tagged Dmp1 and Dmp2 were coexpressed in *E. coli* and purified using Ni-affinity beads.

Table 1 Data collection, phasing and refinement statistics

	Dmp1,2 (Native)	Dmp1,2 (SeMet)			Dmp1,2 Δloop–α5	PAC3 (Native)	PAC3 (SeMet)
Data collection							
Space group	$P3_1$	$P6_322$			$P2_12_12$	$P4_32_12$	$P4_32_12$
Cell dimensions							
a, *b*, *c* (Å)	57.5, 57.5, 82.2	139.1, 139.1, 92.3			158.0, 158.5, 65.2	89.1, 89.1, 57.5	86.6, 86.6, 57.2
		Peak	*Inflection*	*Remote*			
Wavelength	0.9000	0.97925	0.97945	0.96408	0.9000	1.5418	1.5418
Resolution (Å)	1.96 (2.03–1.96)		3.60 (3.73–3.60)		2.90 (3.00–2.90)	2.00 (2.07–2.00)	1.80 (1.86–1.80)
R_{merge}	0.059 (0.187)	0.093 (0.518)	0.073 (0.433)	0.105 (0.551)	0.080 (0.350)	0.084 (0.452)	0.052 (0.479)
$I / \sigma I$	24.6	12.5	13.5	11.3	20.0	14.9	15.7
Completeness (%)	98.0 (93.7)	98.8 (94.9)	84.6 (85.2)	87.2 (87.1)	99.8 (99.9)	99.9 (99.9)	99.2 (98.1)
Redundancy	4.0 (2.6)	6.1 (4.8)	4.3 (3.7)	5.3 (4.7)	6.3 (6.4)	13.2 (12.4)	12.3 (10.8)
Refinement							
Resolution (Å)	49.8–1.96				50.4–2.90	27.5–2.00	
No. reflections	20,240						
R_{work} / R_{free}	0.240 / 0.287				0.250 / 0.283	0.180 / 0.252	
No. atoms							
Protein	2,079				6,604	1883	
Water	31				0	259	
B-factors (Å^2)							
Protein	40.9				66.9	24.8	
Water	37.6					35.8	
r.m.s. deviations							
Bond lengths (Å)	0.010				0.015	0.019	
Bond angles (°)	1.393				1.757	1.663	

Values in parentheses are for highest-resolution shell. One crystal was used for each data set. SeMet, selenomethionine-substituted protein.

Protein extraction. For immunoprecipitation and protein purification, cells were suspended in lysis buffer (50 mM HEPES-KOH (pH 7.6), 100 mM β-glycerolphosphate, 50 mM NaF, 1 mM $MgCl_2$, 1 mM EGTA, 5% (v/v) glycerol and 0.25% (v/v) Triton X-100 containing complete mini EDTA-free protease inhibitors (Roche)). For glycerol gradient analysis and BN-PAGE, cells were suspended in 50 mM HEPES-KOH (pH 7.6), 1 mM $MgCl_2$, 1 mM DTT and 2 mM ATP. Total cell lysates were prepared by vortexing with glass beads using a Multibeads shocker (Yasui Kikai) and cleared by centrifugation at 20,000 × *g* for 10 min at 4 °C.

Detection of polyubiquitinated proteins. Cells were suspended in 200 ml of cold ethanol containing 2 mM PMSF. Cells were lysed by agitation with 200 ml of glass beads for 10 min. Cells lysates were dried and suspended in sample buffer for western blotting. The primary antibody was anti-ubiquitin antibody (Chemicon), and the secondary antibody was anti-mouse IgG-horseradish peroxidase (Jackson ImmunoResearch).

Coimmunoprecipitation of tagged proteins. For **Figure 2e**, cell lysates from YT145 (Dmp1-3×Flag) and YT212 (Dmp1-3×Flag and Dmp2-3×HA) cells were mixed with anti-HA antibodies and incubated for 2 h, after which protein G–Sepharose beads (GE Healthcare) were added and the mixture was incubated for 1 h (left) or cell lysates from YT211 (Dmp2-3×HA) and YT212 (Dmp1-3×Flag and Dmp2-3×HA) were mixed with anti-Flag M2 agarose beads (Sigma) and incubated for 2 h. Then, immunoprecipitates were eluted in lysis buffer containing 200 μg ml^{-1} 3×Flag peptides (Sigma; right).

Glycerol gradient analysis. Cell extracts (2 mg of protein) were separated into 32 fractions by centrifugation (22 h, 100,000 × *g*) in 8–32% (v/v) glycerol linear gradients as described previously[5].

Binding assay. *In vitro* labeling was carried out using the TNT T7 Quick for PCR DNA system (Promega) with ^{35}S-labeled methionine, according to the manufacturer's instructions. Recombinant GST–Dmp1–Dmp2 was expressed in *E. coli* and purified with glutathione-Sepharose beads. The GST–Dmp1–Dmp2–bound beads were added to the labeling mixture and incubated on ice for 1 h. The resulting products were washed with PBS containing 0.5% (v/v) Triton X-100 and eluted using 50 mM Tris-HCl (pH 8.0), 50 mM NaCl, 1 mM EDTA, 1 mM DTT and 10 mM glutathione. The eluates were separated by SDS-PAGE and visualized using autoradiography.

Assay of proteasome activity. Peptidase activity was measured using a fluorescent peptide substrate, succinyl-Leu-Leu-Val-Tyr-7-amino-4-methylcoumarin (Suc-LLVY-AMC), as described previously[5]. A low concentration of SDS (0.025% (w/v)) was used as an artificial activator of 20S proteasomes that are usually latent in cells.

Induction of Dmp2 by galactose. YT596 (*GAL1p-DMP2*, α6-HA) and YT597 (*GAL1p-DMP2*, Δ*dmp1*, α6-HA) cells were grown overnight in 1.5 ml of YPD medium and then cultured in 10 ml of YPG medium to induce the expression of *DMP2* under the *GAL1* promoter. After incubation for 4 h or 8 h, cells were harvested and total cell lysates were subjected to BN-PAGE and immunoblotting with anti-HA antibodies or SDS-PAGE and immunoblotting with anti-Dmp2 antibodies.

Crystallization and data collection. Protein expression and purification were carried out as described in the **Supplementary Methods**. Crystallization of the Dmp1–Dmp2 complex was performed using the hanging-drop vapor diffusion method after mixing 3 μl of protein solution (20 mg ml^{-1}) and 1 μl of reservoir solution containing 25 mM MES (pH 6.5), 50 mM KH_2PO_4 and 16% (w/v) PEG8000. The selenomethionine (SeMet) crystals were grown at 20 °C by mixing 2 μl of protein solution and 2 μl of reservoir solution containing 0.1 M HEPES (pH 7.0) and 4.1 M NaCl. The Dmp1–Dmp2 Δloop–α5 crystals were

prepared using 0.1 M Tris-HCl (pH 8.5), 8% (v/v) ethylene glycol and 12% (w/v) PEG8000. PAC3 was crystallized using the hanging-drop vapor diffusion method after mixing 2 μl of protein solution with 2 μl of reservoir solution containing 0.1 M Tris-HCl (pH 8.5), 0.2 M $MgCl_2$ and 30% (w/v) PEG4000. SeMet PAC3 was similarly crystallized except that the pH was adjusted to 9.1.

Diffraction data sets for wild-type and SeMet Dmp1–Dmp2 as well as Dmp1–Dmp2 Δloop–α5 were collected at 100 K on beamline BL44XU (SPring-8). The diffraction data for native PAC3 and the SeMet derivative were collected using a Rigaku FR-E X-ray generator and a Rigaku R-AXIS VII detector. Data processing and reduction were carried out with the DENZO/SCALEPACK[26]. The crystal forms of wild-type Dmp1–Dmp2, SeMet Dmp1–Dmp2, Dmp1–Dmp2 Δloop–α5 and PAC3 belong to the $P3_1$, $P6_322$, $P2_12_12$, and $P4_32_12$ space groups, respectively. Data collection, phasing and refinement statistics are summarized in **Table 1**.

Structure determination and refinement. The structure of the Dmp1–Dmp2 complex was determined using multiwavelength anomalous diffraction (MAD) and SeMet proteins. The positions of heavy atoms were obtained using SHELXD[27] and refined with SHARP[28]. Initial MAD phases were extended to 3.6 Å and improved with solvent flattening and histogram mapping using DM[29]. The structure of wild-type Dmp1–Dmp2 was determined by molecular replacement using MOLREP[30] with SeMet Dmp1–Dmp2 as a search model. An initial model was built using ARP/wARP[31]. Manual building was then carried out using the program COOT[32] and alternated with several cycles of refinement using the program REFMAC5 (ref. 33).

The structure of Dmp1–Dmp2 Δloop–α5 was determined using the molecular replacement technique MOLREP and the structures of Dmp1–Dmp2 and α5 (PDB ID code 1RYP). The PAC3 structure was solved using the single-wavelength anomalous diffraction (SAD) method and the programs SHELXD and SHARP. Phasing and refinement statistics are summarized in **Table 1**. There are no residues in disallowed regions of the Ramachandran plot. Structure figures were generated using MOLSCRIPT[34], RASTER3D[35], and CCP4MG[36].

Accession codes. Protein Data Bank: Coordinates have been deposited under accession numbers 2Z5B for Dmp1–Dmp2, 2Z5C for Dmp1–Dmp2–α5 and 2Z5E for PAC3.

Note: Supplementary information is available on the Nature Structural & Molecular Biology website.

ACKNOWLEDGMENTS

We thank all of the members of BL44XU, especially E. Yamashita and M. Yoshimura, for their help in data collection at SPring-8 and T. Hikage for his help in X-ray diffraction data collection for PAC3. This work was supported by grants from Japan Science and Technology Agency (to S.M.), the Ministry of Education, Culture, Sports, Science and Technology (MEXT) of Japan (to H.Y., T.M., S.M., E.K., K.K. and K. Tanaka) and the Target Protein Project of MEXT (to T.M., K.K. and K. Tanaka and the Takeda Science Foundation (to K. Tanaka)). E.S. is a recipient of a Japan Society for the Promotion of Science Research Fellowship for Young Scientists.

AUTHOR CONTRIBUTIONS

H.Y. and T. Kameyama performed all of the yeast experiments. T.M., H.Y., K. Takagi and T.Y. determined the structures of the Dmp1–Dmp2 and Dmp1–Dmp2 Δloop–α5 complexes. K.O., E.K., E.S., A.S., Y.H., S.M., T.Y. and K.K. determined the structure of PAC3. H.H., T. Kishimoto and S.N. conducted the mass spectrometric analysis. M.K. performed phylogenetic analyses. H.Y., T.M., K.K., M.K. and K. Tanaka wrote the paper. All of the authors discussed the results and commented on the manuscript.

Published online at http://www.nature.com/nsmb/
Reprints and permissions information is available online at http://npg.nature.com/reprintsandpermissions

1. Baumeister, W., Walz, J., Zuhl, F. & Seemuller, E. The proteasome: paradigm of a self-compartmentalizing protease. *Cell* **92**, 367–380 (1998).
2. Coux, O., Tanaka, K. & Goldberg, A.L. Structure and functions of the 20S and 26S proteasomes. *Annu. Rev. Biochem.* **65**, 801–847 (1996).
3. Zwickl, P., Kleinz, J. & Baumeister, W. Critical elements in proteasome assembly. *Nat. Struct. Biol.* **1**, 765–770 (1994).
4. Chen, P. & Hochstrasser, M. Biogenesis, structure and function of the yeast 20S proteasome. *EMBO J.* **14**, 2620–2630 (1995).
5. Hirano, Y. *et al.* A heterodimeric complex that promotes the assembly of mammalian 20S proteasomes. *Nature* **437**, 1381–1385 (2005).
6. Nandi, D., Woodward, E., Ginsburg, D.B. & Monaco, J.J. Intermediates in the formation of mouse 20S proteasomes: implications for the assembly of precursor β subunits. *EMBO J.* **16**, 5363–5375 (1997).
7. Li, X., Kusmierczyk, A.R., Wong, P., Emili, A. & Hochstrasser, M. β-Subunit appendages promote 20S proteasome assembly by overcoming an Ump1-dependent checkpoint. *EMBO J.* **26**, 2339–2349 (2007).
8. Ramos, P.C., Hockendorff, J., Johnson, E.S., Varshavsky, A. & Dohmen, R.J. Ump1p is required for proper maturation of the 20S proteasome and becomes its substrate upon completion of the assembly. *Cell* **92**, 489–499 (1998).
9. Hirano, Y. *et al.* Cooperation of multiple chaperones required for the assembly of mammalian 20S proteasomes. *Mol. Cell* **24**, 977–984 (2006).
10. Burri, L. *et al.* Identification and characterization of a mammalian protein interacting with 20S proteasome precursors. *Proc. Natl. Acad. Sci. USA* **97**, 10348–10353 (2000).
11. Heink, S., Ludwig, D., Kloetzel, P.M. & Kruger, E. IFN-γ-induced immune adaptation of the proteasome system is an accelerated and transient response. *Proc. Natl. Acad. Sci. USA* **102**, 9241–9246 (2005).
12. Jayarapu, K. & Griffin, T.A. Protein-protein interactions among human 20S proteasome subunits and proteassemblin. *Biochem. Biophys. Res. Commun.* **314**, 523–528 (2004).
13. Bachmair, A., Finley, D. & Varshavsky, A. *In vivo* half-life of a protein is a function of its amino-terminal residue. *Science* **234**, 179–186 (1986).
14. Johnson, E.S., Ma, P.C., Ota, I.M. & Varshavsky, A. A proteolytic pathway that recognizes ubiquitin as a degradation signal. *J. Biol. Chem.* **270**, 17442–17456 (1995).
15. Meimoun, A. *et al.* Degradation of the transcription factor Gcn4 requires the kinase Pho85 and the SCF(CDC4) ubiquitin-ligase complex. *Mol. Biol. Cell* **11**, 915–927 (2000).
16. Mannhaupt, G., Schnall, R., Karpov, V., Vetter, I. & Feldmann, H. Rpn4p acts as a transcription factor by binding to PACE, a nonamer box found upstream of 26S proteasomal and other genes in yeast. *FEBS Lett.* **450**, 27–34 (1999).
17. Xie, Y. & Varshavsky, A. RPN4 is a ligand, substrate, and transcriptional regulator of the 26S proteasome: a negative feedback circuit. *Proc. Natl. Acad. Sci. USA* **98**, 3056–3061 (2001).
18. Glickman, M.H. *et al.* Functional analysis of the proteasome regulatory particle. *Mol. Biol. Rep.* **26**, 21–28 (1999).
19. Fehlker, M., Wendler, P., Lehmann, A. & Enenkel, C. Blm3 is part of nascent proteasomes and is involved in a late stage of nuclear proteasome assembly. *EMBO Rep.* **4**, 959–963 (2003).
20. Schmidt, M. *et al.* The HEAT repeat protein Blm10 regulates the yeast proteasome by capping the core particle. *Nat. Struct. Mol. Biol.* **12**, 294–303 (2005).
21. Groll, M. *et al.* Structure of 20S proteasome from yeast at 2.4 Å resolution. *Nature* **386**, 463–471 (1997).
22. Unno, M. *et al.* The structure of the mammalian 20S proteasome at 2.75 Å resolution. *Structure* **10**, 609–618 (2002).
23. Tallec, B. *et al.* 20S Proteasome assembly is orchestrated by two distinct pairs of chaperones in yeast and in mammals. *Mol. Cell* **27**, 660–674 (2007).
24. Tanaka, K. *et al.* Proteasomes (multi-protease complexes) as 20 S ring-shaped particles in a variety of eukaryotic cells. *J. Biol. Chem.* **263**, 16209–16217 (1988).
25. Takeuchi, J., Fujimuro, M., Yokosawa, H., Tanaka, K. & Toh-e, A. Rpn9 is required for efficient assembly of the yeast 26S proteasome. *Mol. Cell. Biol.* **19**, 6575–6584 (1999).
26. Otwinowski, Z. & Minor, W. Processing of x-ray diffraction data collected in oscillation mode. *Methods Enzymol.* **276**, 307–326 (1997).
27. Schneider, T.R. & Sheldrick, G.M. Substructure solution with SHELXD. *Acta Crystallogr. D Biol. Crystallogr.* **58**, 1772–1779 (2002).
28. Bricogne, G., Vonrhein, C., Flensburg, C., Schiltz, M. & Paciorek, W. Generation, representation and flow of phase information in structure determination: recent developments in and around SHARP 2.0. *Acta Crystallogr. D Biol. Crystallogr.* **59**, 2023–2030 (2003).
29. CCP4. The CCP4 suite: programs for protein crystallography. *Acta Crystallogr. D Biol. Crystallogr.* **50**, 760–763 (1994).
30. Vagin, A.A. & Teplyakov, A. MOLREP: an automated Program for molecular replacement. *J. Appl. Crystallogr.* **30**, 1022–1025 (1997).
31. Morris, R.J., Perrakis, A, & Lamzin, V.S. ARP/wARP and automatic interpretation of protein electron density maps. *Methods Enzymol.* **374**, 229–244 (2003).
32. Emsley, P. & Cowtan, K. Coot: model-building tools for molecular graphics. *Acta Crystallogr. D Biol. Crystallogr.* **60**, 2126–2132 (2004).
33. Murshudov, G.N., Vagin, A.A. & Dodson, E.J. Refinement of macromolecular structures by the maximum-likelihood method. *Acta Crystallogr. D Biol. Crystallogr.* **53**, 240–255 (1997).
34. Kraulis, P.J. MOLSCRIPT: a program to produce both detailed and schematic plots of protein structures. *J. Appl. Crystallogr.* **24**, 946–950 (1991).
35. Merritt, E.A. & Murphy, M.E. Raster3D Version 2.0. A program for photorealistic molecular graphics. *Acta Crystallogr. D Biol. Crystallogr.* **50**, 869–873 (1994).
36. Potterton, E., McNicholas, S., Krissinel, E., Cowtan, K. & Noble, M. The CCP4 molecular-graphics project. *Acta Crystallogr. D Biol. Crystallogr.* **58**, 1955–1957 (2002).

THE JOURNAL OF BIOLOGICAL CHEMISTRY VOL. 283, NO. 33, pp. 22847–22857, August 15, 2008

Structural Basis for Sorting Mechanism of p62 in Selective Autophagy*

Received for publication, March 19, 2008, and in revised form, May 19, 2008 Published, JBC Papers in Press, June 4, 2008, DOI 10.1074/jbc.M802182200

Yoshinobu Ichimura[‡1], Taichi Kumanomidou[§1], Yu-shin Sou[‡¶1], Tsunehiro Mizushima[§], Junji Ezaki[‡], Takashi Ueno[‡], Eiki Kominami[‡], Takashi Yamane[§], Keiji Tanaka[¶], and Masaaki Komatsu[‡¶‖2]

From the [‡]Department of Biochemistry, Juntendo University School of Medicine, Bunkyo-ku, Tokyo 113-8421, the [§]Department of Biotechnology, Graduate School of Engineering, Nagoya University, Chikusa-ku, Nagoya 464-8603, the [¶]Laboratory of Frontier Science, Tokyo Metropolitan Institute of Medical Science, Bunkyo-ku, Tokyo 113-8613, and [‖]PRESTO, Japan Science and Technology Corporation, Kawaguchi 332-0012, Japan

Impairment of autophagic degradation of the ubiquitin- and LC3-binding protein "p62" leads to the formation of cytoplasmic inclusion bodies. However, little is known about the sorting mechanism of p62 to autophagic degradation. Here we identified a motif of murine p62 consisting of 11 amino acids (Ser^{334}–Ser^{344}) containing conserved acidic and hydrophobic residues across species, as an LC3 recognition sequence (LRS). The crystal structure of the LC3-LRS complex at 1.56 Å resolution revealed interaction of Trp^{340} and Leu^{343} of p62 with different hydrophobic pockets on the ubiquitin fold of LC3. *In vivo* analyses demonstrated that p62 mutants lacking LC3 binding ability accumulated without entrapping into autophagosomes in the cytoplasm and subsequently formed ubiquitin-positive inclusion bodies as in autophagy-deficient cells. These results demonstrate that the intracellular level of p62 is tightly regulated by autophagy through the direct interaction of LC3 with p62 and reveal that selective turnover of p62 via autophagy controls inclusion body formation.

Macroautophagy (hereafter referred to as autophagy) is a major pathway for intracellular bulk degradation by the lysosome/vacuole, and its molecular machinery is highly conserved among eukaryotes. In the autophagic process, a small membrane sac (called isolation membrane) elongates to enwrap cytoplasmic materials, including organelles, and subsequently the extended membrane closes to form a double-membrane structure termed autophagosome. The autophagosome fuses with the lysosome/vacuole where the sequestered cytoplasmic contents within the autophagosome are degraded by hydrolases of the lysosome/vacuole (1, 2). This system is required to execute turnover of cytosolic proteins and for removal of unwanted organelles (*e.g.* called as pexophagy, mitophagy, and reticulophagy).

Genetic and molecular studies in the yeast *Saccharomyces cerevisiae* have identified 18 *ATG* (autophagy-related genes) essential for autophagosome formation (1). Among them, eight *ATG* products include two ubiquitin-like conjugation systems essential for autophagy (3, 4). Atg12 is a ubiquitin-like protein covalently linked to Atg5 by catalytic reactions of Atg7 (ubiquitin-activating enzyme) and Atg10 (ubiquitin-conjugating enzyme) (5). Atg12-Atg5 interacts with Atg16, resulting in oligomerization of Atg12-Atg5·Atg16 (6). Another ubiquitin-like protein, Atg8 conjugates to a phosphatidylethanolamine (PE).[3] Atg8, synthesized as a precursor form with extra amino acid residues, is processed by Atg4 cysteine protease, which exposes a glycine residue at its C terminus (7). The processed Atg8 is conjugated to PE by Atg7 (ubiquitin-activating enzyme) and Atg3 (ubiquitin-conjugating enzyme) (8). Furthermore, recent studies have revealed that Atg12-Atg5 conjugate functions as a ubiquitin ligase-like enzyme for Atg8 lipidation reaction (9). Finally, the C-terminal glycine of Atg8 covalently conjugates to an amino group of PE (8). Atg8-PE mediates membrane tethering and hemifusion involving the formation of autophagosomal membrane, and its level correlates with autophagosome formation (10). The mammalian Atg8 homologs, microtubule-associated protein 1 light chain 3 (LC3), $GABA_A$ receptor-associated protein (GABARAP), and Golgi-associated ATPase enhancer of 16 kDa (GATE-16), are also conjugated to PE via the same ubiquitin-like system to Atg8 lipidation (11–13).

In recent years, it has become clear that autophagy plays an important role in a variety of physiological responses as follows: starvation, development, differentiation, tumorigenesis, immunity, and neurodegeneration (1). Autophagy, particularly that responsive to starvation, is generally considered a nonselective degradation (1). This large scale degradation enables cells to survive during starvation by recycling of the degradation products for sources of energy production and macromolecule synthesis. In addition to the starvation-induced adaptive autoph-

* This work was supported by grants from the Japan Science and Technology Agency (to M. K.), the Ministry of Education, Science and Culture of Japan (to M. K. and K. T.), the Target Protein Project of Ministry of Education, Science and Culture of Japan (to T. M. and K. T.), and Takeda Science Foundation (to K. T.). The costs of publication of this article were defrayed in part by the payment of page charges. This article must therefore be hereby marked "*advertisement*" in accordance with 18 U.S.C. Section 1734 solely to indicate this fact.

The atomic coordinates and structure factors (code 2ZJD) have been deposited in the Protein Data Bank, Research Collaboratory for Structural Bioinformatics, Rutgers University, New Brunswick, NJ (http://www.rcsb.org/).

[1] These authors contributed equally to this work.

[2] To whom correspondence should be addressed. Tel.: 81-3-3823-2105; Fax: 81-3-3823-2237; E-mail: mkomatsu@rinshoken.or.jp.

[3] The abbreviations used are: PE, phosphatidylethanolamine; LRS, LC3 recognition sequence; LC3, microtubule-associated protein 1 light chain 3; GABARAP, γ-aminobutyric acid, type A, receptor-associated protein; GATE-16, Golgi-associated ATPase enhancer of 16 kDa; MBP, maltose-binding protein; GST, glutathione *S*-transferase; CBB, Coomassie Brilliant Blue; MEF, mouse embryonic fibroblast; GFP, green fluorescent protein; Dox, doxycycline; PB1, Phox and Bem1p.

agy, growing lines of evidence point to the importance of basal autophagy that operates constitutively at low rates even under a nutrient-rich environment and plays a vital role in the maintenance of cellular homeostasis (14–17). Indeed, studies using mouse genetics have indicated that autophagy-deficient mice exhibit remarkable accumulation of ubiquitinated protein aggregates followed by hepatocytic and neuronal cell death irrespective of nutrient stresses (14, 15, 17).

p62 is a scaffold protein involved in multiple signaling pathways and is present in ubiquitin-related inclusions such as those seen in liver injury and various neurodegenerative diseases (*e.g.* alcoholic hepatitis, steatohepatitis, Huntington disease, Parkinson disease, and amyotrophic lateral sclerosis) (18–20). Importantly, we have found recently that p62 is a preferred target for autophagy, and intracellular levels of p62 are constantly controlled by constitutive autophagy (21, 22). In addition, previous studies revealed that p62 directly interacts with LC3, an autophagosome marker protein (21, 23). However, little is known molecularly about how p62 is sorted into autophagosomes. In addition to this issue, although we showed that homeostatic levels of p62 control ubiquitin-positive inclusion body formation at the cytoplasm in hepatocytes and neurons of autophagy-deficient mice (21), it is still unclear whether inclusion formation is only because of deficiency in p62 turnover. In other words, the molecular relationship between autophagic removal of p62 and inclusion body formation remains to be uncovered.

This study was designed to shed light on the aforementioned issues related to p62, LC3, autophagosome, inclusion formation, and autophagy. We report the identification of LC3 recognition sequence (LRS) of p62, which includes 11 amino acids (Ser^{334}–Ser^{344}), and the crystal structure of LC3-LRS complex, clarifying the interaction mode at the molecular level. Further biochemical and genetic analyses using autophagy- and/or p62-deficient mouse cells demonstrated that autophagic degradation of p62 absolutely depends on the interaction of LC3, and that the impairment of the physical interaction leads to the formation of cytosolic inclusion bodies. The results indicate that p62 is essential for inclusion body formation associated with impaired autophagy.

EXPERIMENTAL PROCEDURES

Plasmid Construction—Maltose-binding protein (MBP) fused p62 (MBP-p62), and its deletion mutant (MBP-p62M7) expression plasmids have been described previously (21). To construct p62M7 variants, a series of deletions of p62M7 were amplified by PCR using appropriate primers and cloned into the MBP fusion expression plasmid, pMALp2 (New England Biolabs). Glutathione *S*-transferase (GST)-fused LC3B expression plasmid has been described previously (13). Point mutations were inserted by the QuikChange site-directed mutagenesis kit (Stratagene) according to the protocol supplied by the manufacturer. All constructs were confirmed by DNA sequencing with BigDye terminator cycle sequencing ready reaction kit version 1.1 (Applied Biosystems).

Purification of Recombinant Proteins for Pulldown Experiments—MBP-tagged p62 and mutants were expressed in *Escherichia coli* strain BL21 Star (DE3) (Invitrogen) by induction of 0.05 mM isopropyl β-D-thiogalactopyranoside at 25 °C for 16 h. The cells were lysed in bacterial protein extraction reagent (Pierce) at room temperature for 10 min. Insoluble proteins were removed by centrifugation at 15,000 rpm for 10 min by microcentrifuge. The cell extracts were diluted 1:5 into TBS (20 mM Tris-HCl, pH 7.5, and 150 mM NaCl) and incubated with amylose resin (New England Biolabs) at 4 °C for 2 h. The MBP fusion protein-bound amylose resins were washed three times with TBS. The MBP-p62 and mutants were eluted with TBS containing 10 mM maltose. The purity was confirmed on SDS-polyacrylamide gel followed by Coomassie Brilliant Blue (CBB) staining (SimplyBlue SafeStain (Invitrogen)). GST-tagged LC3, its mutants GABARAP and GATE-16, were purified in a manner similar to that described above except for affinity purification using glutathione-Sepharose 4B (Amersham Biosciences). For removal of the GST region, PreScission protease cleavage was performed (Amersham Biosciences). Protein concentrations were determined by BCA protein assay reagent (Pierce).

Pulldown Assay—MBP-p62 and its mutants were expressed in *E. coli* BL21 Star (DE3), and the cell extracts were prepared by bacterial protein extraction reagent. The cell extracts were diluted 5-fold with TBS and incubated with amylose resin (New England Biolabs). The MBP-p62 and its mutants immobilized amylose resin were washed extensively with TBS. The resulting immobilized amylose resins containing about 5 μg of MBP fusion proteins were incubated with 15 μg of LC3 family proteins (LC3, GABARAP, or GATE-16) in 50 μl of TBS on ice for 1 h, and then washed three times with 500 μl of TBS. Bound proteins with amylose resins were suspended into SDS-PAGE sample buffer and subjected to SDS-PAGE followed by CBB staining. GST pulldown was performed through the same procedures described above, except that GST fusion was immobilized on glutathione-Sepharose 4B (Amersham Biosciences), and MBP-p62M7 was introduced in this assay.

Protein Expression and Purification for Crystal Structure—GST-tagged LC3 was expressed from pGEX6P plasmid in BL21 (RIPL). The protein was purified using glutathione-Sepharose 4B and cation exchange chromatography. The GST moiety was proteolytically removed by PreScission protease. The protein solution was concentrated to 18.6 mg/ml by ultrafiltration in 25 mM Tris-HCl, pH 7.5, and 1 mM dithiothreitol. The concentrated LC3 was mixed with LRS peptide representing residues ^{334}SGGDDDWTHLS^{344} from p62 with equal molar ratio and incubated for 3 h.

Crystallization and Data Collection—Crystals of LC3-LRS peptide complex were obtained at 15 °C by the hanging-drop vapor-diffusion method, with a mixture of 2.0 μl of protein and the same volume of reservoir solution (0.1 M HEPES, pH 7.5, and 25% w/v polyethylene glycol 3,350). Although crystals formed in 2 days, they were not sufficient for crystal structure determination. Initial crystals were used to generate larger crystals by microseeding. During the microseeding experiments, the concentration of the precipitant was varied. Single crystals suitable for x-ray diffraction measurement were finally obtained with reservoir conditions consisting of 0.1 M HEPES, pH 7.5, and 23% w/v polyethylene glycol 3,350. Crystals were transferred to cryoprotective solution containing 10% v/v glyc-

TABLE 1
Data collection and refinement statistics
Values in parentheses represent highest resolution shell.

	LC3-p62 (334–344)
Data collection	
Space group	$P2_1$
Cell dimensions	
a, *b*, *c* (Å)	45.6, 39.6, 78.0
α, β, γ (°)	90.0, 93.3, 90.0
Wavelength (Å)	0.9000
Resolution (Å)	1.55 (1.61-1.55)
Total reflections	179,556
Unique reflections	39,943
Completeness (%)	98.4 (86.0)
$I/\sigma(I)$	23.9
Multiplicity	4.5 (4.2)
R_{merge}	0.054 (0.310)
Refinement	
Resolution range (Å)	77.85–1.56
R_{work}/R_{free}	0.199/0.237
Root mean square deviation	
Bonds (Å)	0.010
Angles (°)	1.298

erol, 0.1 M HEPES, pH 7.5, and 23% w/v polyethylene glycol 3,350 for 30 s.

Diffraction data sets for the LC3-p62 complex were collected at 100 K on beamline BL44XU (SPring-8, Japan). Data processing and reduction were carried out with the DENZO/SCALEPACK (36). The crystal forms of LC3-p62 complex belong to the $P2_1$ space group and two molecules in the asymmetric unit. Data collection, phasing, and refinement statistics are summarized in Table 1.

Structure Determination and Refinement—The structure of the LC3-p62 complex was determined by molecular replacement using MOLREP (32) with LC3 (PDB ID code 1UGM) (29) as a search model. An initial model was constructed using ARP/wARP (37). Manual building was then carried out using the program XtalView (38) and altered with several cycles of refinement using the program REFMAC5 (39). The final refined model consists of residues 2–122 and residues 1–122 of the molecules in the asymmetric unit. For the p62 peptide, the density allowed building 10 residues complexed to one molecule and 7 residues complexed to the second molecule. Phasing and refinement statistics are summarized in Table 1. There were no residues in the disallowed regions of the Ramachandran plot. Structure figures were generated using CCP4MG (40) and PyMOL (41).

Generation of Tet-On Cells—Immortalized *p62-* and *Atg7/p62*-deficient mouse embryonic fibroblasts (MEFs) were established by infecting MEFs with a recombinant retrovirus carrying a temperature-sensitive simian virus 40 large T antigen (42). Tetracycline-mediated p62-expressing cell lines were generated using the reverse tetracycline-regulated retroviral vector (43). A cassette consisting of the gene-encoding packaging signal (ψ), the reverse tetracycline-controlled transactivator (rtTA), the internal ribosome entry site from the encephalomyocarditis virus, the blasticidin S deaminase, a heptamerized tetracycline operator sequence (tetO), the minimal human cytomegalovirus immediate early promoter designated P_{hcmv}*-1 (CMV), and green fluorescent protein (GFP)-fused mouse p62 cDNA or various p62 mutants (p62W340A, p62L343A, p62D338A/D339A, and p62D337A/D338A/D339A) were cloned into a Moloney murine leukemia virus retroviral vector pLXSN backbone (43). Retrovirus packaging cells, PLAT-E (44), transfected with the vectors were cultured at 37 °C for 24 h. After changing the medium, the virus producing PLAT-E was further incubated at 37 °C for 24 h. The viral supernatant was collected and used immediately for infection. The immortalized *p62-* and *Atg7/p62*-deficient MEFs were plated on 35-mm dishes in 3 ml of growth medium at 24 h before infection. Just before infection, the medium was replaced with undiluted viral supernatant with 8 μg/ml Polybrene (Sigma). Twenty four hours later, the cells were introduced into the selection medium containing 5 μg/ml of blasticidin S (Invitrogen). The cells remaining after 5 days were used in the experiments. To induce the expression of p62, the cells were treated with 250 μg/ml of doxycycline (Dox, Sigma) for 24 h.

Immunological Analysis—MEFs were lysed with lysis buffer (10 mM Tris-Cl, pH 7.4, 150 mM NaCl, Complete protease inhibitor mixture (Roche Diagnostics), and 2% Triton X-100). The lysates were centrifuged at 15,000 rpm for 5 min at 4 °C, and the resultant supernatant was analyzed by immunoblotting. The antibodies for p62, Atg7, and LC3 were described previously (21). The antibody for actin (MAB1501R) was purchased from Chemicon International. For immunofluorescence microscopy, MEFs grown on glass coverslips were immunostained with anti-LC3 (21) and anti-ubiquitin antibodies (FK2, MBL) as described previously (21).

Accession Codes—Protein Data Bank: The coordinates and structure factors for LC3-LRS complex have been deposited under accession code 2ZJD.

RESULTS

LC3-interacting Region of p62—p62 is composed of three domains as follows; N-terminal Phox and Bem1 (PB1) domain, zinc finger domain (Zinc), and C-terminal ubiquitin-associated (UBA) domain (19, 20). Several reports have suggested that p62 can directly interact with LC3, thereby possibly sequestering p62 into the autophagosome (21, 23). We have shown previously that LC3 interacts with a linker region (named M7 domain) between the zinc finger and UBA domain in mouse p62 (21). To determine the minimal region of p62M7-(168–391) required for the interaction with LC3, we performed pulldown assay experiments using a series of deletion mutants of p62M7. Initially, we examined six mutants of truncated p62M7 (M71–M76) (Fig. 1*A*). Each MBP-fused p62M7 mutant (M71–M76), which was immobilized on amylose resins, was incubated with recombinant LC3B (hereafter referred to as LC3), washed extensively, and subjected to SDS-PAGE followed by CBB staining. LC3 was clearly detected in pulldown products with p62 mutants harboring the M76 region (334–391) but not the M72 region (168–333), suggesting that p62M76-(334–391) is sufficient for the interaction with LC3 (Fig. 1*B*). To shorten the interaction domain, we subsequently prepared a deletion series of p62M76 (M77–M82) for MBP pulldown assay. These pulldown assays revealed that p62M82, which includes 11 amino acids (334–344), is essential and sufficient for LC3 interaction (Fig. 1*B*). p62M82, which we named LRS (LC3 recognition sequence), contains two conserved motifs across species as

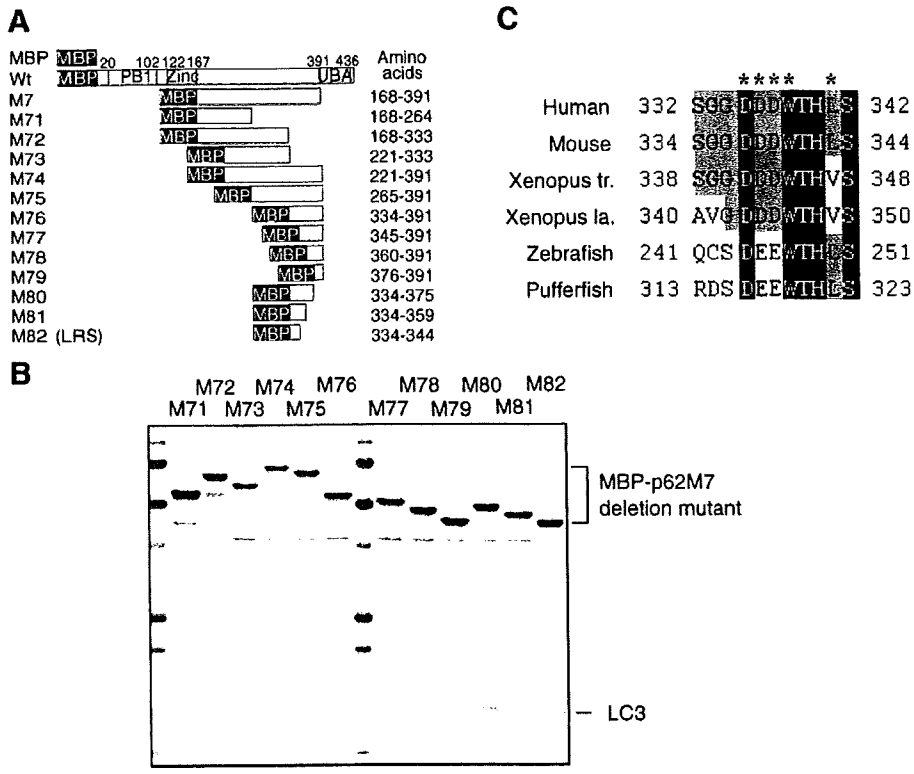

FIGURE 1. **Identification of LC3-interacting region in p62.** *A*, diagrams of deletion-mutation constructs of p62 used for the pulldown assay. The MBP-tagged mouse p62(Wt) and its deletion mutants p62M7 have been described previously (21). Deletions of M7 (M71–M82) were generated by PCR amplifications and fused to the C terminus of MBP. Phox and Bem1p (*PB1*), zinc finger (*Zinc*), and ubiquitin-associated (*UBA*) domains are represented. LRS; LC3 recognition sequence means the LC3 binding region (334–344) in p62. *B*, MBP pulldown assay. MBP-p62M7 deletion mutants conjugated with amylose resins were incubated with purified recombinant LC3. The pulled down complex with MBP-p62M7 mutants was subjected to SDS-PAGE and visualized by CBB staining. *C*, LRS alignment of p62 homologs in various species. *Asterisks* indicate LC3-interacting residues; *black* and *gray boxes* indicate identical amino acid residues with complete and partial conservation, respectively.

follows: acidic cluster (337–339) DDD (or DEE) and hydrophobic residues (340 and 343) W*XX*L (or W*XX*V) involved in protein-protein interaction (Fig. 1*C* and see also Fig. 2).

Overall Structure of the LC3-LRS Complex—Based on the above results, we determined the structure of LC3-LRS complex by x-ray crystallography. The complex consists of a full-length LC3-(1–125) bound to the LRS of p62-(334–344). The crystal structure of the LC3-LRS complex was determined by molecular replacement using C-terminal truncated LC3-I (residues 1–120, PDB code 1UGM) and refined to 1.56 Å resolution (Fig. 2*A*). The final model consists of residues 2–122 and residues 1–122 of the two molecules in the asymmetric unit (molecules A and B), respectively. The structure of LRS-bound LC3, which consists of a five-stranded β-sheet and five α-helices, is essentially identical to the previously reported structures of peptide-free LC3-I; these structures have an average 1.15 Å root mean square deviation for the C-α positions, although several differences are evident. The LRS binds to one side of the LC3 surface opposite the C-terminal region. Of the 11 residues in the LRS crystals, only 10- and 7-residue segments (molecule A, 335–344; molecule B, 338–344) are ordered in the structure. The LC3 surface has a narrow channel, and the LRS binds within the LC3 groove in an extended conformation (Fig. 2*B*).

The LRS-binding surface consists of three α-helices (α1, α2, and α3) and two β-strands (β1 and β2). A total of 601 Å^2 of accessible surface area is buried at the interface between the LC3 and LRS. The most striking feature of the interactions is that the indole ring of Trp^{340} is inserted into a site surrounded by a conserved group of hydrophilic and hydrophobic residues, Asp^{19}, Ile^{23}, Pro^{32}, Lys^{51}, Leu^{53}, and Phe^{108} (Fig. 2, *B–D*). The second major interaction is between Leu^{343} of LRS and the β1, β2, and α3 of LC3. Leu^{343} makes van der Waals contacts with Ile^{35}, Phe^{52}, Val^{54}, Leu^{63}, and Ile^{66} and the aliphatic portion of the Arg^{70} (Fig. 2, *B–D*). The third interaction site is between the N-terminal portion of LRS and the basic cluster (Arg^{10}, Arg^{11}, and Lys^{49}) on the surface of LC3. A group of charged and hydrophilic residues are present in the contact area for both interacting partners that could potentially form a series of salt bridges and hydrogen bonds between the two molecules. These hydrophilic contacts include Asp^{337} and Asp^{338} from LRS and Arg^{10} and Arg^{11} of LC3. In addition, the peptide is coordinated by several hydrogen bonds involving Asp^{337}, Thr^{341}, Leu^{343}, and Ser^{344} of LRS and Lys^{51}, Leu^{53}, and Arg^{69} of LC3.

To confirm the interacting structure of LC3-LRS, point mutation was inserted into the indicated amino acids of LRS in p62M7 by replacement with alanine (Fig. 2*E*). MBP pulldown assay showed that the formation of the LC3-p62M7 complex was significantly reduced in W340A and L343A mutants (Fig. 2*E*). Likewise, the interaction with LC3 was almost abolished in D337A/D338A, D338A/D339A, and D337A/D338A/D339A mutants (Fig. 2*E*). These results indicate that the hydrophobic (Trp^{340} and Leu^{343}) and acidic cluster (Asp^{337}–Asp^{339}) of p62 are important for LC3 binding. The structure of LC3-LRS suggests that the LRS associates with many amino acids of LC3. In the next step, we introduced mutation in a number of these amino acids of LC3 critically involved in the interaction with LRS as follows: R10A, R11A, K51A, F52A, L53A, I66A, R70A, and N-terminal helix deletion ($\Delta\alpha$1 or $\Delta\alpha$1-α2), followed by GST pulldown assay (Fig. 2*F*). As predicted from the crystal structure of the complex, the series of GST-LC3 mutants tested were significantly compromised in their ability to pull down MBP-p62M7 (Fig. 2*F*). These results are in agreement with the above results of crystal structure analysis.

Predicted Structures of Atg8 Homolog-LRS Complex—The sequence homology between LC3 and other Atg8 homologs suggests that LRS may also bind to other Atg8 homologs (Fig.

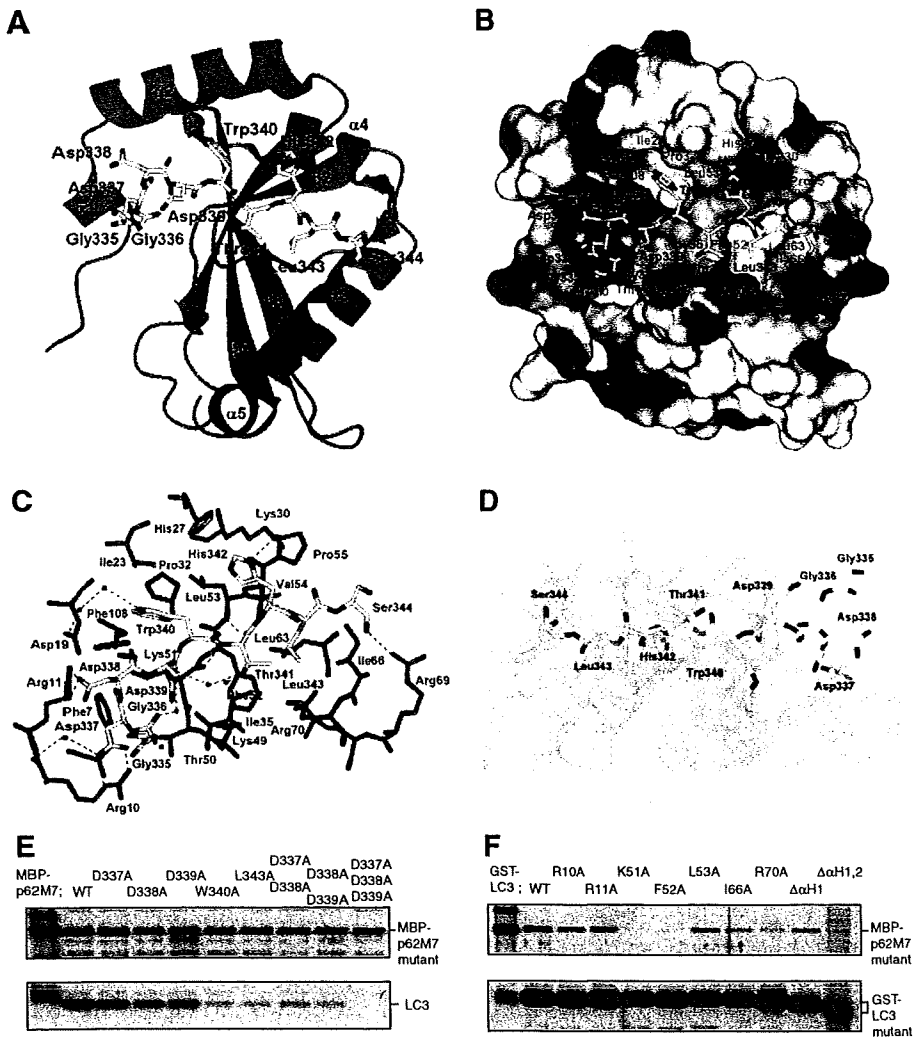

FIGURE 2. **Structure of the LC3-p62 peptide complex.** *A*, overall structure of the complex. *Green*, LC3 color; *yellow*, p62 peptide (LRS). The secondary structure elements (α1–α5 helices and β1–β5 sheets) for LC3 are labeled. *B*, electrostatic surface representation of the p62-binding site of the LC3 with the LRS. The surface is colored according to the electrostatic potential (*blue*, positive; *red*, negative). Residues from LC3 that interact with p62 are labeled in *green*. *C*, close-up view of the LC3-LRS interface showing amino acids of LC3 (*green*), LRS (*yellow*), and water molecules (*red*). *Dashed lines*, hydrogen bonds. *D*, side view with partial transparency of the LC3-LRS interaction. Stick of LRS (*yellow*) is shown within the groove of LC3 molecular surface (partially *transparent gray*). *E*, pulldown assay with p62M7 mutants. MBP-p62M7 mutants immobilized amylose resin, and purified LC3 was incubated, and the pulled down products were subjected to SDS-PAGE followed by CBB staining. *F*, pulldown assay with LC3 mutants. GST-LC3 mutants immobilized glutathione-Sepharose 4B, and purified p62M7 were incubated, and then the pulled down products were subjected to SDS-PAGE followed by CBB staining.

homologs have a similar affinity for p62 in the *in vitro* condition.

Interaction between LC3 and p62 Is Indispensable for in Vivo Autophagic Degradation of p62—To investigate the degradation mode of p62 by autophagy (*i.e.* via interaction with LC3) *in vivo*, we took advantage of the Tet-On system (Fig. 4*A*). The Tet-On/Tet-Off system allows regulation of reversible and quantitative gene expression in cells. The Tet-On system is widely used to induce gene expression by treatment of cells with tetracycline or its analog Dox (26). We prepared a regulator gene cassette, CAG-rtTA and TRE-GFP-fused wild type and a series of p62 mutants (W340A, L343A, D338A/D339A, and D337A/D338A/D339A), and then introduced them into immortalized *p62* knock-out and *Atg7/p62* double knock-out mouse embryonic fibroblasts (MEFs) to abolish the effect of endogenous wild-type p62. The presence of Dox in the culture medium should induce the expression of GFP-p62 and the mutants, whereas Dox removal should allow suppression of the expression (Fig. 4*A*). To examine the degradation of p62, the cells were cultured in media containing Dox for 24 h, and then the level of GFP-p62 was chased for 36 h by culturing Dox-free media. Both wild-type and mutant GFP-p62 were efficiently expressed in each cells (Fig. 4, *B* and *C*). Removal of Dox markedly decreased the expression of wild-type GFP-p62 in $p62^{-/-}$ MEFs by 12 h, and this fall was time-dependent, and only small amounts of GFP-p62 (9.76%) remained at 36 h after removal of Dox. In contrast, such down-regulation was trivial and insignificant in *Atg7/p62* double knock-out MEFs (Fig. 4, *B* and *C*); 75.9% of GFP-p62 remained even at 36 h after removal of Dox in double knock-out MEFs. These results indicate that the degradation of GFP-p62 is mainly dependent on the autophagy pathway. When the mutant forms of GFP-p62, which has a slight binding capacity to LC3 (Fig. 2*E*), were expressed into $p62^{-/-}$ MEFs, the rates of the degradation were much slower compared with that of wild-type p62 (Fig. 4, *B* and *C*). The percentages of p62W340A, p62L343A, p62D338A/D339A, and p62D337A/D338A/D339A remaining at 36 h after removal of Dox were 44.6, 48.1, 49.0, and 49.6%, respectively. However, these remaining levels were still lower than that of

3*A*). To elucidate the binding mode between LRS peptide and Atg8 homologs, the complex models of GABARAP-LRS and GATE-16-LRS were created from the rat GABARAP (24) and bovine GATE-16 (25) structures, respectively, by using the MOE program (version 2005.06; Chemical Computing Group, Montreal, Canada) (Fig. 3, *C* and *D*). In these models, although GABARAP and GATE-16 form the major interaction sites of Trp^{340} and Leu^{343}, the basic surface on α1 helix of LC3 interacting with the acidic cluster of Asp^{337}–Asp^{339} are different from those of the corresponding GABARAP and GATE-16 region (Fig. 2*B* and Fig. 3, *C* and *D*). However, MBP pulldown assay showed the equivalent interactions of p62M7 with LC3, GABARAP, and GATE-16 (Fig. 3*B*) suggesting that Atg8

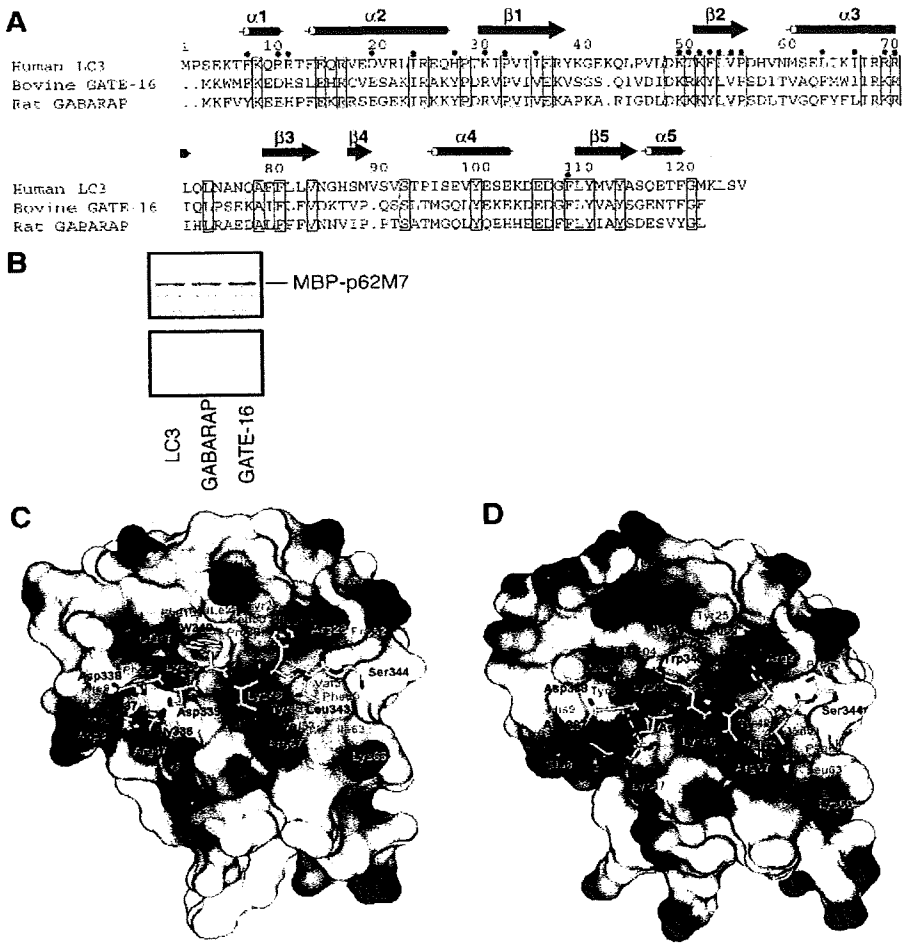

FIGURE 3. **Comparison of LC3 and its homologs.** *A*, sequence alignments of human LC3, rat GABARAP, and bovine GATE-16. Identical amino acid residues are *boxed*. The secondary structural element of LC3 is indicated *above* the alignments. LC3 interacting residues of p62 peptide are indicated by *red circles*. *B*, interaction of p62M7 and LC3 homologs. MBP-p62M7 conjugated with amylose resins were incubated with purified LC3, GABARAP, and GATE-16. The pulled down products with MBP-p62M7 were detected in CBB-stained SDS-PAGE. *C* and *D*, models of the GATE-16-p62 peptide and GABARAP-p62 peptide complex from published structures (codes 1eo6 and 1kgt). GATE-16 and GABARAP are shown in electrostatic surface representation. p62 peptide is shown as a *stick model*. Residues that correspond to residues from LC3 shown in Fig. 2*B* are labeled.

GFP-p62 in *Atg7/p62* double knock-out MEFs, implying partial defect in degradation of these mutants. Interestingly, an *in vitro* binding assay revealed no significant difference in the LC3-binding ability among p62 mutants except for the triple D337A/D338A/D339A mutant accompanied with severely reduced LC3 interaction (Fig. 2*E*). However, these degradation rates *in vivo* were almost similar, suggesting equal contribution among hydrophobic (Trp^{340} and Leu^{343}) and acidic (Asp^{337}–Asp^{339}) clusters of p62 on LC3 interaction *in vivo*. Taken together, these *in vivo* results strongly suggest that loss of interaction between LC3 and p62 is sufficient to impair the degradation of p62.

PB1 Domain of p62 Is Important for Efficient Degradation of p62 via Autophagy—The PB1 domains are scaffold modules that adopt the topology of ubiquitin-like β-grasp folds with the interaction of each other in a front-to-back mode to arrange heterodimers or homo-oligomers (27). Actually, p62 can polymerize via the PB1 domain (28). To examine the roles of the PB1 domain in autophagic degradation of p62, we expressed a K7A/D69A mutant of p62, which compromises the interaction surface of the PB1 domain, accompanied with loss of self-oligomerization activity (28), in $p62^{-/-}$ MEFs using the Tet-On system, and then compared the degradation rate of the mutant with that of wild-type p62. Surprisingly, this mutation was accompanied by significantly degradative delay, compared with wild-type p62 (Fig. 4, *D* and *E*). The percentages of wild-type and p62K7A/D69A remaining at 36 h after removal of Dox was 7.80 and 36.9%, respectively. However, the degradation rate of p62K7A/D69A in $p62^{-/-}$ MEFs was still higher than that in *Atg7/p62* double knock-out MEFs, indicating that the defective oligomerization form of p62 is still degraded, at least in part, by the autophagy pathway (Fig. 4, *D* and *E*). Actually, additional mutation of p62 lacking LC3 interaction accelerated the delay of degradation (Fig. 4, *D* and *E*). These results suggest that in addition to LC3 interaction, self-oligomerization of p62 is required for effective degradation of p62 via autophagy.

Impairment of LC3-p62 Interaction Causes Ubiquitin- and p62-positive Inclusion Formation—Finally, we investigated the cellular localization of wild-type p62 and the mutants. Consistent with previous studies (21, 22), immunofluorescent analysis with anti-LC3 antibody showed localization of GFP-p62 in cup-shaped and dot structures in GFP-p62-expressing *p62* knock-out MEFs. These structures were always positive for LC3 (Fig. 5*A*). Impairment of p62 turnover by autophagy deficiency causes accumulation of p62-positive inclusion (21). Indeed, 20–30% of *Atg7/p62* double knock-out GFP-p62-expressing MEFs contained GFP-p62-positive inclusions characterized by their large sizes and positive staining for anti-ubiquitin (Fig. 5*B*). Similarly, expression of GFP-p62 mutants, which have lower ability to associate with LC3 (Fig. 2*E*), was associated with the formation of p62-positive inclusions, although these inclusions were almost negative for LC3 (Fig. 5*A*). Moreover, ubiquitinated proteins were also present in the structures (Fig. 5*B*). In *p62* knock-out MEFs expressing GFP-p62, only a few ubiquitin-positive dots were detected in autophagosomes positive for GFP-p62, suggesting that the ubiquitin-positive aggregates in MEFs might be trapped into autophagosomes before they become large aggregates/inclusions. Both auto-

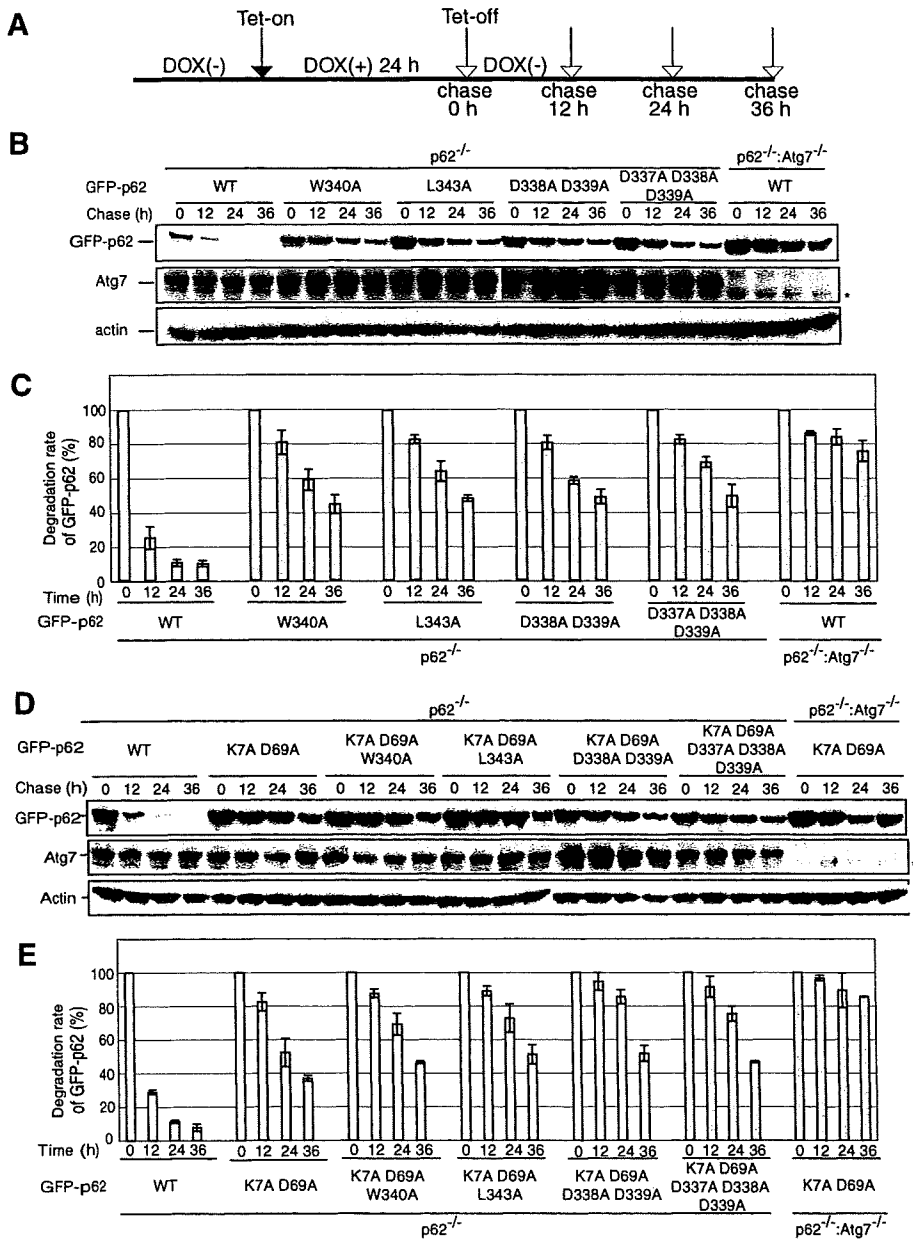

FIGURE 4. **Turnover of p62 is dependent on interaction with LC3 and p62.** *A*, schematic representation of experiments conducted to monitor p62 protein level. Immortalized *p62* and *Atg7/p62* knock-out MEFs were introduced with two regulator gene cassettes, CAG-rtTA and TRE-GFP-fused wild type and a series of mutant p62 (p62W340A, p62L343A, p62D338AD339A and p62D337AD338AD339A) with or without PB1 mutation (K7AD69A). These cells were cultured for 24 h in the presence of Dox to induce expression of GFP-p62 or the mutants. Subsequently, the cells were cultured in the absence of Dox and lysed at the times indicated by *white arrows*. *B*, immunoblot analysis of GFP-p62. The cell lysates were prepared at various time points after transient expression of GFP-p62 and the mutants and then subjected to SDS-PAGE followed by immunoblotting with the indicated antibodies. Data are representative of three separate experiments. *Asterisk*, nonspecific band. *C*, quantitative densitometry of immunoblotting data shown in *B* and the ratios of p62 relative to actin. *D*, immunoblot analysis of GFP-p62 with PB1 mutation. GFP-p62K7AD69A with or without mutation of LC3 interaction was expressed into immortalized *p62* and *Atg7/p62* knock-out MEFs and analyzed as shown in *A*. *E*, quantitative densitometry of immunoblotting data shown in *D* and the ratios of p62 relative to actin.

phagosome formation and degradation of long lived proteins in *p62* knock-out cells are apparently comparable with those in wild-type cells (21). These results therefore indicate that impairment of p62-LC3 interaction alone is sufficient for the formation of ubiquitin- and p62-positive inclusions, *i.e.* loss of the interaction triggers inclusion body formation.

Based on the possible oligomerization in PB1 domain and the ubiquitin-binding ability in the UBA domain of p62, it is postulated that PB1 plays an important role in inclusion formation, including polyubiquitinated proteins. Indeed, when GFP-p62K7AD69A lacking self-oligomerization activity was expressed into *Atg7/p62* double knock-out MEFs, inclusion formation observed in those expressing wild-type p62 was completely suppressed (Fig. 5*C*), strongly suggesting the essential role of the PB1 domain in inclusion formation (for details see "Discussion").

DISCUSSION

We have reported recently that the intracellular level of p62 is controlled by constitutive autophagic degradation, and impairment of such a process causes significant accumulation of inclusion bodies containing p62 and ubiquitinated proteins (21). Furthermore, we and Pankiv *et al.* (21, 23) found that p62 interacts directly with LC3, an autophagosome marker protein. These reports imply that p62 could be targeted to the autophagosome through interaction with LC3 for degradation of itself together with ubiquitinated proteins. However, information on the sorting mechanism(s) for p62 is not available at present.

We originally identified the LRS consisting of 11 amino acids in p62. The short peptide of p62, LRS, allowed us to determine the crystal structure of the LC3-LRS complex. The tertiary structure of LC3-LRS revealed that both acidic cluster (DDD or DEE) and hydrophobic motif (W*XX*L or W*XX*V) in LRS are highly conserved among species and involved in the interaction with LC3. Recently, Pankiv *et al.* (23) reported the LC3 interacting region (LIR) consisting of 22 amino acids (Arg^{321}–Ser^{342}) in human p62. In comparison, the LRS (Ser^{334}–Ser^{344}) in murine p62 described in the present study is shorter than the LIR but corresponds exactly to the

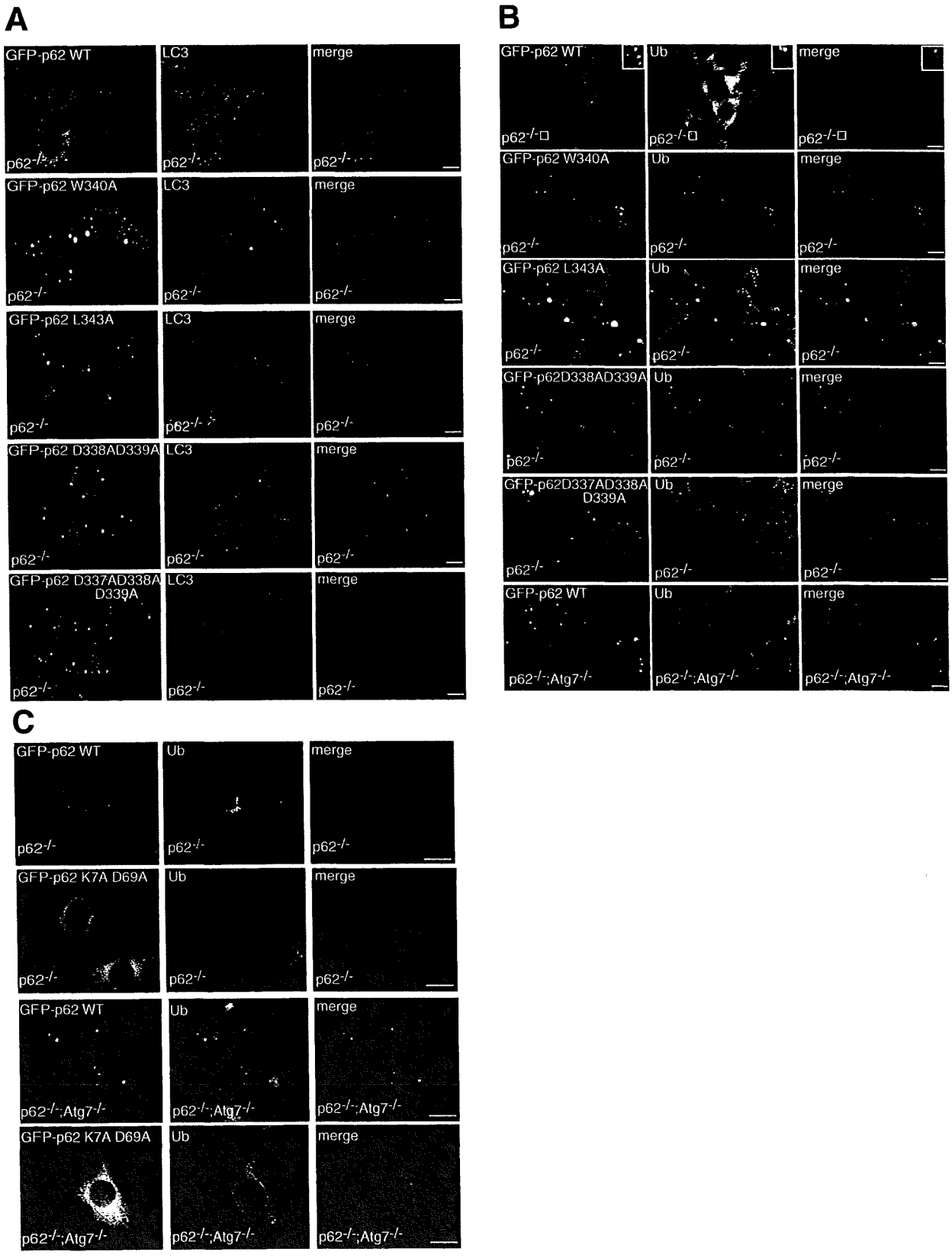

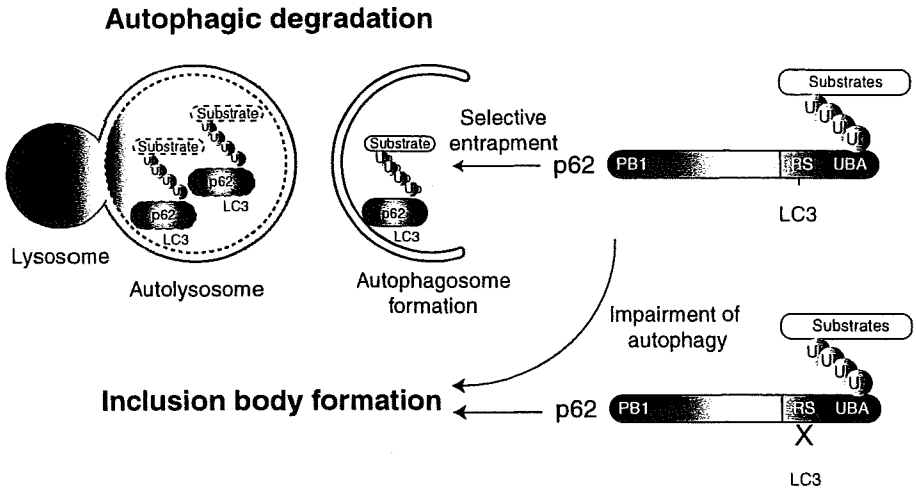

FIGURE 6. **Schematic model for selective autophagy mediated by p62.** p62 was dissected into three domains in the context of the present study, *i.e.* N-terminal PB1 for self-oligomerization, LRS for LC3 interaction, and C-terminal UBA for ubiquitin binding domains. Ubiquitinated proteins initially interact with the UBA domain and are selectively entrapped into autophagosomes through interaction between LRS and LC3 for their degradation under normal conditions. Because PB1 mutant (K7A/D69A) lacking self-oligomerization ability was associated with decreased degradation of itself, oligomerization of p62 might be needed for effective turnover of p62. On the other hand, impaired turnover of p62 (*e.g.* genetic loss of autophagy or mutation of LRS in p62 in our hand) causes accumulation of p62 associated with ubiquitinated proteins, resulting in high cytoplasmic levels of p62, which presumably promote self-oligomerization of p62 via the PB1 domain. Subsequently, those oligomer complexes segregate and form inclusion bodies in the cytoplasm to reduce the cytotoxic effects of soluble and/or oligomerized proteins. Note that the LRS mutant of p62 lacking LC3 binding ability induces significant inclusion body formation, analogous to that in autophagy-deficient cells. Accordingly, the interaction between LC3 and p62 is a key event in selective autophagy that contributes to the aggressive removal of unfavorable ubiquitinated proteins in cells.

C-terminal region of LIR (23). In addition, their mapping of the sites involved in LC3 interaction is also essentially similar to our results except the importance of Leu^{343} residue found in our study (23).

The structure of LC3 includes a C-terminal ubiquitin fold and N-terminal two α-helices (29). In this study, we identified a new functional molecular surface composed of N-terminal basic residues and two hydrophobic pockets at the ubiquitin domain of LC3 as p62-interacting regions. The two distinct hydrophobic pockets were present close to each other on the surface of the ubiquitin fold and just localized at the interface of the complex. Previous mutational analyses of Atg8 identified the critical residues involved in autophagosomal membrane formation (10, 30). Intriguingly, Lys^{48}–Leu^{50} of Atg8, essential for autophagosome formation after PE conjugation reaction, corresponds to Lys^{51}–Leu^{53} existing in the two hydrophobic pockets of LC3 (10, 30). Similarly, the N-terminal two α-helices of LC3, corresponding to the region involved in tethering and hemifusion function of Atg8, are also required for p62 interaction (10). These results suggest that both autophagosome formation and p62 recognition utilize a common hydrophobic patch on the LC3 surface.

The structure of GABARAP has been shown in two conformations as follows: one is the N-terminal α-helix connected to the ubiquitin domain (closed), and the other is the N-terminal α-helix projected away from ubiquitin domain (open) (31). Furthermore, we have proposed that PE conjugation induces conformation change in the N-terminal α-helices of Atg8, and the open form is active conformation for hemifusion (10). These findings suggest that the region of the N-terminal α-helices of Atg8 is flexible. Because the structure of the LC3-LRS complex exists in a form in which basic residues of the N-terminal of LC3 bind to the acidic cluster of LRS, the LC3 N-terminal α-helices might be stabilized as a closed (or inactive) form. Conceivably, the two distinct conformations with the N terminus of LC3 may be related to the underlying molecular functions such as membrane expansion and/or sorting receptor in autophagy.

Structure comparison of LRS-bound LC3 homologs has shown high similarity and LRS structurally aligned on the two hydrophobic pockets on their ubiquitin fold surface (24, 25, 29). Interestingly, the basic amino acids in the N-terminal helices of LC3 are not found in those of other Atg8 homologs, suggesting that LC3 might have a higher affinity for p62 than other homologs. However, we have not detected any differences among LC3 homologs in the *in vitro* pulldown experiments, implying the similar affinity of LC3 homologs for p62. Although GABARAP and GATE-16 share common biochemical characteristics with LC3 and localize to autophagosomes (3, 12), their behaviors responding to nutrient conditions differ among Atg8 homologs (17). Further analysis is required to unravel the structural relationship of interaction between Atg8 homologs and p62.

We have shown that autophagy deficiency leads to marked accumulation of p62- and ubiquitin-positive inclusion, and p62 is indispensable for such inclusion formation (21). Importantly, p62 is a major component of ubiquitin-containing inclusions known as the "hepatocytic Mallory body" found in alcoholic hepatitis and steatohepatitis (32). Similar structures have been identified also as proteinaceous aggregates in the remnant neu-

FIGURE 5. **Impairment of p62-LC3 interaction is sufficient to induce the formation of ubiquitin- and p62-positive inclusions.** *A*, immunofluorescence analysis of cellular localization of GFP-p62 and LC3. *p62* knock-out MEFs were fixed at 36 h after transient expression of GFP-p62 and the mutants and then immunostained with anti-LC3 antibody. *Right panels*, merged images. *Bar*, 10 μm. *B*, immunofluorescence analysis of cellular localization of GFP-p62 and ubiquitin. *p62* or *p62/Atg7* knock-out MEFs were fixed as shown in *A* and then immunostained with anti-ubiquitin antibody. *Right panels*, merged images. Higher magnification views in *top panels* are shown in *insets*. *Bar*, 10 μm. *C*, immunofluorescence analysis of cellular localization of GFP-p62 and GFP-p62K7A/D69A. *Atg7/p62* knock-out MEFs were fixed at 36 h after transient expression of GFP-p62 or GFP-p62K7A/D69A and then immunostained with anti-ubiquitin antibody. *Right panels*, merged images. *Bar*, 10 μm.

rons in various neurodegenerative disorders such as Parkinson disease and amyotrophic lateral sclerosis (33, 34). In such diseases, it is plausible that the reduced autophagic activity is associated with the formation of inclusion bodies. This possibility is also supported by the results of a recent study using CHMP2B mutants (35). However, it remains unclear whether only impairment of p62 turnover through autophagy is responsible for the formation of inclusion bodies. Our analyses using the Tet-On system clearly showed delayed degradation of p62 mutants lacking LC3 interaction when they were expressed in *p62* knock-out MEFs, resulting in the formation of inclusions containing ubiquitinated proteins. It is noteworthy that autophagosome formation and degradation of long lived proteins in *p62* knock-out cells are comparable with those in wild-type cells (21). Therefore, it seems that only impairment of p62-LC3 interaction is responsible for ubiquitin- and p62-positive inclusion formation.

How is p62 involved in the formation of ubiquitin-positive inclusion? Currently, it is known that the UBA domain of p62 interacts with ubiquitinated proteins (19, 20, 23). However, ubiquitin-tagged proteins are not aggregation-prone themselves. Therefore, it is plausible that excess accumulation of p62 interacting with ubiquitinated protein might predispose to form inclusions via the PB1 domain, which retains the ability of self-oligomerization. Indeed, p62 having PB1 mutation (K7A/D69A), which is defective in self-oligomerization, did not form inclusions in *Atg7* knock-out cells, and then the ubiquitinated proteins remained dispersed, indicating that oligomerization of p62 through the PB1 domain is critical for ubiquitin-positive inclusion in autophagy-deficient cells.

Therefore, it is clear that under physiological conditions, ubiquitinated proteins initially interact with p62 via the UBA domain, and are subsequently selectively entrapped into the autophagosomes through LRS-LC3 interaction for their degradation (see the schematic illustration in Fig. 6, *top panel*). On the other hand, impaired autophagy under certain pathological conditions leads to the accumulation of p62-ubiquitinated protein complexes followed by oligomerization via the PB1 domain, ultimately leading to the formation of inclusion body that presumably contributes to the segregation of harmful and/or unnecessary proteins within the cell (Fig. 6, *bottom panel*). This scenario is in agreement with the previous observations that almost all inclusions in autophagy-deficient cells were positive for both p62 and ubiquitin (21), and reduction of p62 protein level increased cell death when a harmful mutant of Huntingtin was overexpressed (22). Taken together, our results indicate that p62 directly binds to LC3 and is targeted to constitutive and selective autophagy to maintain an intracellular homeostatic level of p62.

Acknowledgments—We thank T. Kouno for the excellent technical assistance; Dr. N. Furuya for helpful discussion; Dr. T. Kitamura (Tokyo University) for providing the PLAT-E cells; Dr. M. Hagiwara (Tokyo Medical and Dental University) for providing the pLRT-X retrovirus vectors; and Dr. Z. Yue (Mount Sinai School of Medicine) for the critical reading of the manuscript.

REFERENCES

1. Levine, B., and Klionsky, D. J. (2004) *Dev. Cell* **6,** 463–477
2. Mizushima, N. (2007) *Genes Dev.* **21,** 2861–2873
3. Ohsumi, Y. (2001) *Nat. Rev. Mol. Cell Biol.* **2,** 211–216
4. Suzuki, K., and Ohsumi, Y. (2007) *FEBS Lett.* **581,** 2156–2161
5. Mizushima, N., Noda, T., Yoshimori, T., Tanaka, Y., Ishii, T., George, M. D., Klionsky, D. J., Ohsumi, M., and Ohsumi, Y. (1998) *Nature* **395,** 395–398
6. Kuma, A., Mizushima, N., Ishihara, N., and Ohsumi, Y. (2002) *J. Biol. Chem.* **277,** 18619–18625
7. Kirisako, T., Ichimura, Y., Okada, H., Kabeya, Y., Mizushima, N., Yoshimori, T., Ohsumi, M., Takao, T., Noda, T., and Ohsumi, Y. (2000) *J. Cell Biol.* **151,** 263–276
8. Ichimura, Y., Kirisako, T., Takao, T., Satomi, Y., Shimonishi, Y., Ishihara, N., Mizushima, N., Tanida, I., Kominami, E., Ohsumi, M., Noda, T., and Ohsumi, Y. (2000) *Nature* **408,** 488–492
9. Hanada, T., Noda, N. N., Satomi, Y., Ichimura, Y., Fujioka, Y., Takao, T., Inagaki, F., and Ohsumi, Y. (2007) *J. Biol. Chem.* **282,** 37298–37302
10. Nakatogawa, H., Ichimura, Y., and Ohsumi, Y. (2007) *Cell* **130,** 165–178
11. Kabeya, Y., Mizushima, N., Ueno, T., Yamamoto, A., Kirisako, T., Noda, T., Kominami, E., Ohsumi, Y., and Yoshimori, T. (2000) *EMBO J.* **19,** 5720–5728
12. Kabeya, Y., Mizushima, N., Yamamoto, A., Oshitani-Okamoto, S., Ohsumi, Y., and Yoshimori, T. (2004) *J. Cell Sci.* **117,** 2805–2812
13. Sou, Y. S., Tanida, I., Komatsu, M., Ueno, T., and Kominami, E. (2006) *J. Biol. Chem.* **281,** 3017–3024
14. Hara, T., Nakamura, K., Matsui, M., Yamamoto, A., Nakahara, Y., Suzuki-Migishima, R., Yokoyama, M., Mishima, K., Saito, I., Okano, H., and Mizushima, N. (2006) *Nature* **441,** 885–889
15. Komatsu, M., Waguri, S., Chiba, T., Murata, S., Iwata, J., Tanida, I., Ueno, T., Koike, M., Uchiyama, Y., Kominami, E., and Tanaka, K. (2006) *Nature* **441,** 880–884
16. Komatsu, M., Ueno, T., Waguri, S., Uchiyama, Y., Kominami, E., and Tanaka, K. (2007) *Cell Death Differ.* **14,** 887–894
17. Komatsu, M., Waguri, S., Ueno, T., Iwata, J., Murata, S., Tanida, I., Ezaki, J., Mizushima, N., Ohsumi, Y., Uchiyama, Y., Kominami, E., Tanaka, K., and Chiba, T. (2005) *J. Cell Biol.* **169,** 425–434
18. Zatloukal, K., Stumptner, C., Fuchsbichler, A., Heid, H., Schnoelzer, M., Kenner, L., Kleinert, R., Prinz, M., Aguzzi, A., and Denk, H. (2002) *Am. J. Pathol.* **160,** 255–263
19. Moscat, J., Diaz-Meco, M. T., and Wooten, M. W. (2007) *Trends Biochem. Sci.* **32,** 95–100
20. Seibenhener, M. L., Geetha, T., and Wooten, M. W. (2007) *FEBS Lett.* **581,** 175–179
21. Komatsu, M., Waguri, S., Koike, M., Sou, Y. S., Ueno, T., Hara, T., Mizushima, N., Iwata, J., Ezaki, J., Murata, S., Hamazaki, J., Nishito, Y., Iemura, S., Natsume, T., Yanagawa, T., Uwayama, J., Warabi, E., Yoshida, H., Ishii, T., Kobayashi, A., Yamamoto, M., Yue, Z., Uchiyama, Y., Kominami, E., and Tanaka, K. (2007) *Cell* **131,** 1149–1163
22. Bjørkøy, G., Lamark, T., Brech, A., Outzen, H., Perander, M., Overvatn, A., Stenmark, H., and Johansen, T. (2005) *J. Cell Biol.* **171,** 603–614
23. Pankiv, S., Clausen, T. H., Lamark, T., Brech, A., Bruun, J. A., Outzen, H., Øvervatn, A., Bjørkøy, G., and Johansen, T. (2007) *J. Biol. Chem.* **282,** 24131–24145
24. Bavro, V. N., Sola, M., Bracher, A., Kneussel, M., Betz, H., and Weissenhorn, W. (2002) *EMBO Rep.* **3,** 183–189
25. Paz, Y., Elazar, Z., and Fass, D. (2000) *J. Biol. Chem.* **275,** 25445–25450
26. Gossen, M., and Bujard, H. (1992) *Proc. Natl. Acad. Sci. U. S. A.* **89,** 5547–5551
27. Moscat, J., Diaz-Meco, M. T., Albert, A., and Campuzano, S. (2006) *Mol. Cell* **23,** 631–640
28. Lamark, T., Perander, M., Outzen, H., Kristiansen, K., Øvervatn, A., Michaelsen, E., Bjørkøy, G., and Johansen, T. (2003) *J. Biol. Chem.* **278,** 34568–34581
29. Sugawara, K., Suzuki, N. N., Fujioka, Y., Mizushima, N., Ohsumi, Y., and Inagaki, F. (2004) *Genes Cells* **9,** 611–618
30. Amar, N., Lustig, G., Ichimura, Y., Ohsumi, Y., and Elazar, Z. (2006)